

Ultra-High Energy Cosmic Rays: Some phenomenological and theoretical Aspects

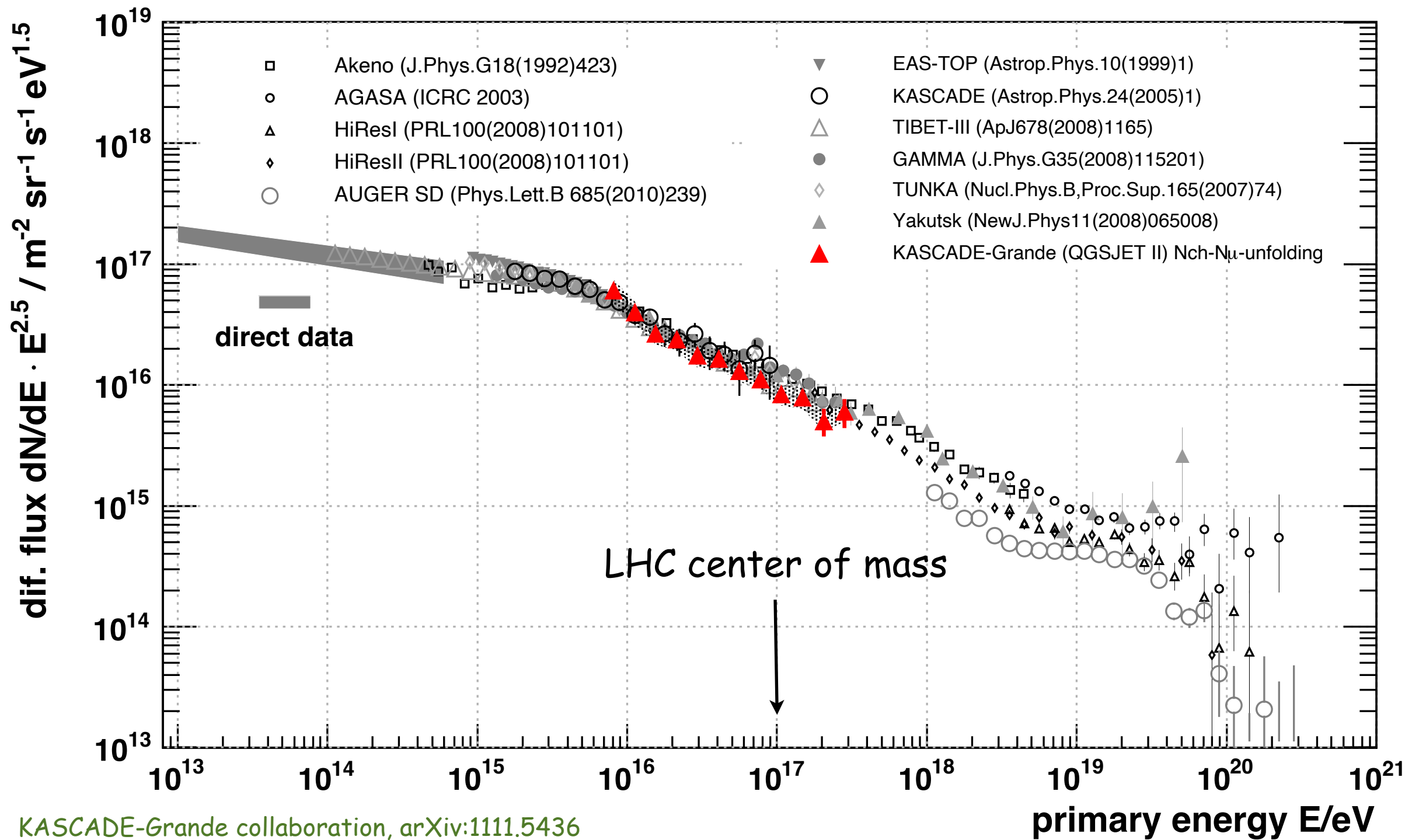
1. Observations
2. Basics and Source Properties
3. Anisotropies and Mass Composition
4. The Muon Excess
5. Lorentz Symmetry Violations

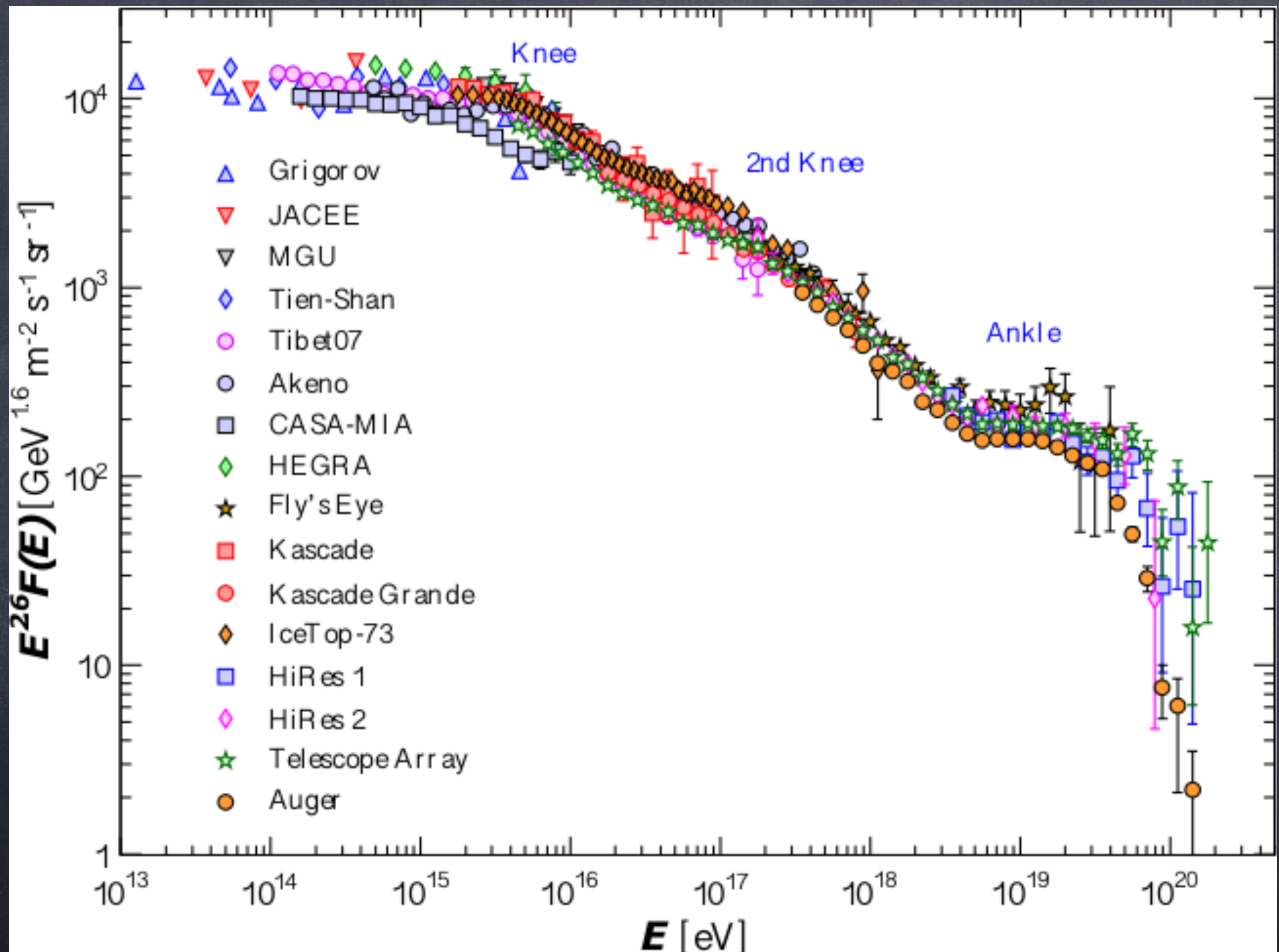


Günter Sigl

II. Institut theoretische Physik, Universität Hamburg

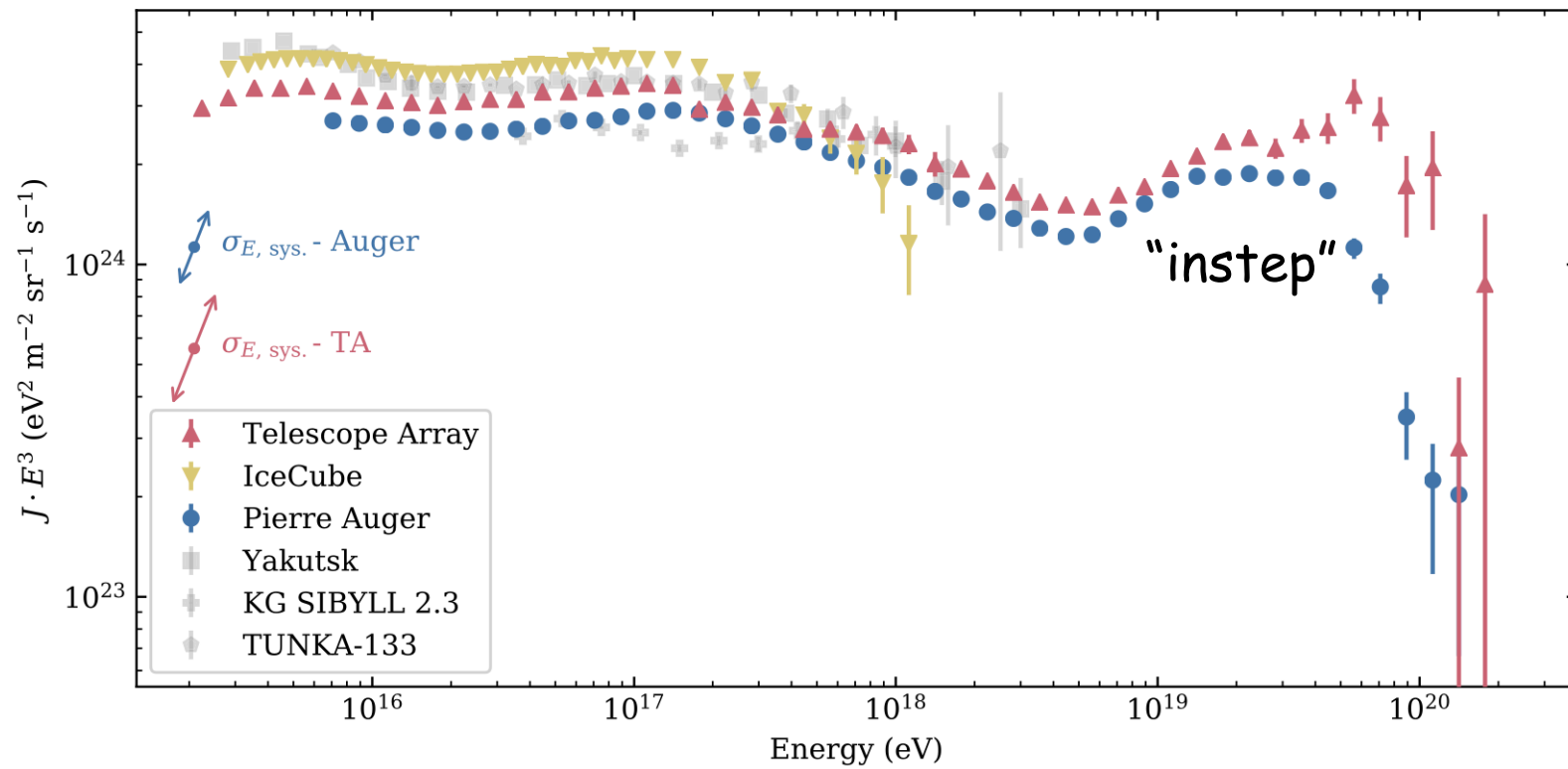
The All Particle Cosmic Ray Spectrum





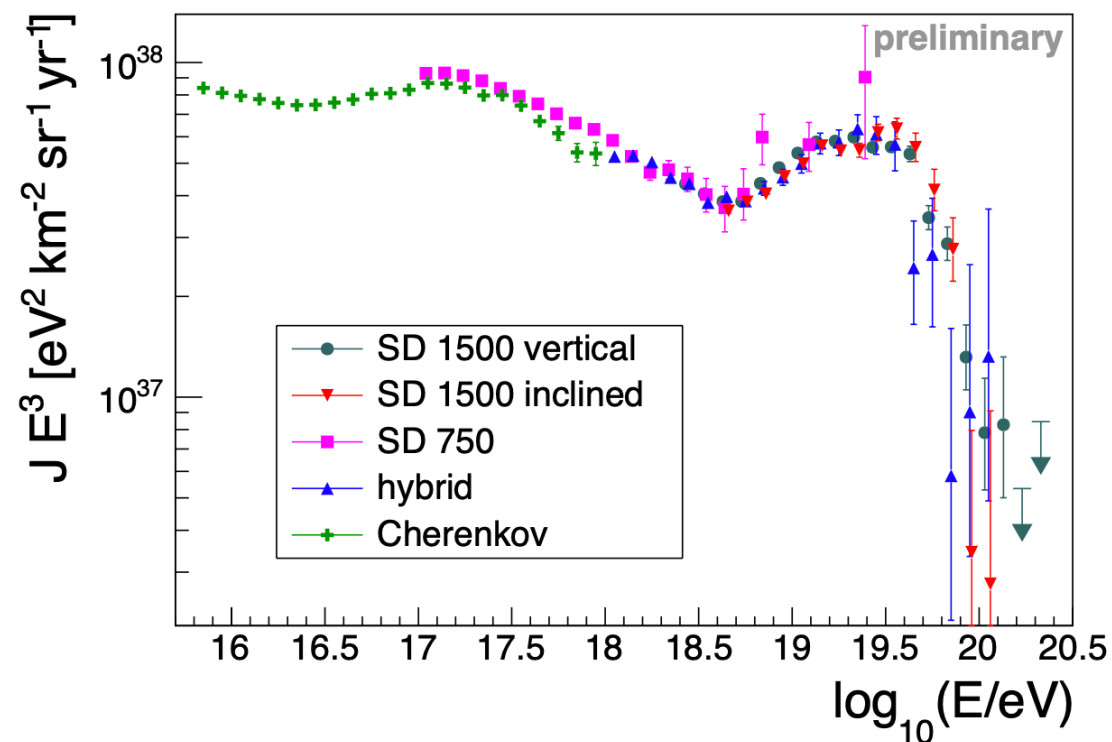
Pierre Auger Spectra

Auger exposure = 60,400 km² sr yr (surface detector vertical) as of end 2018



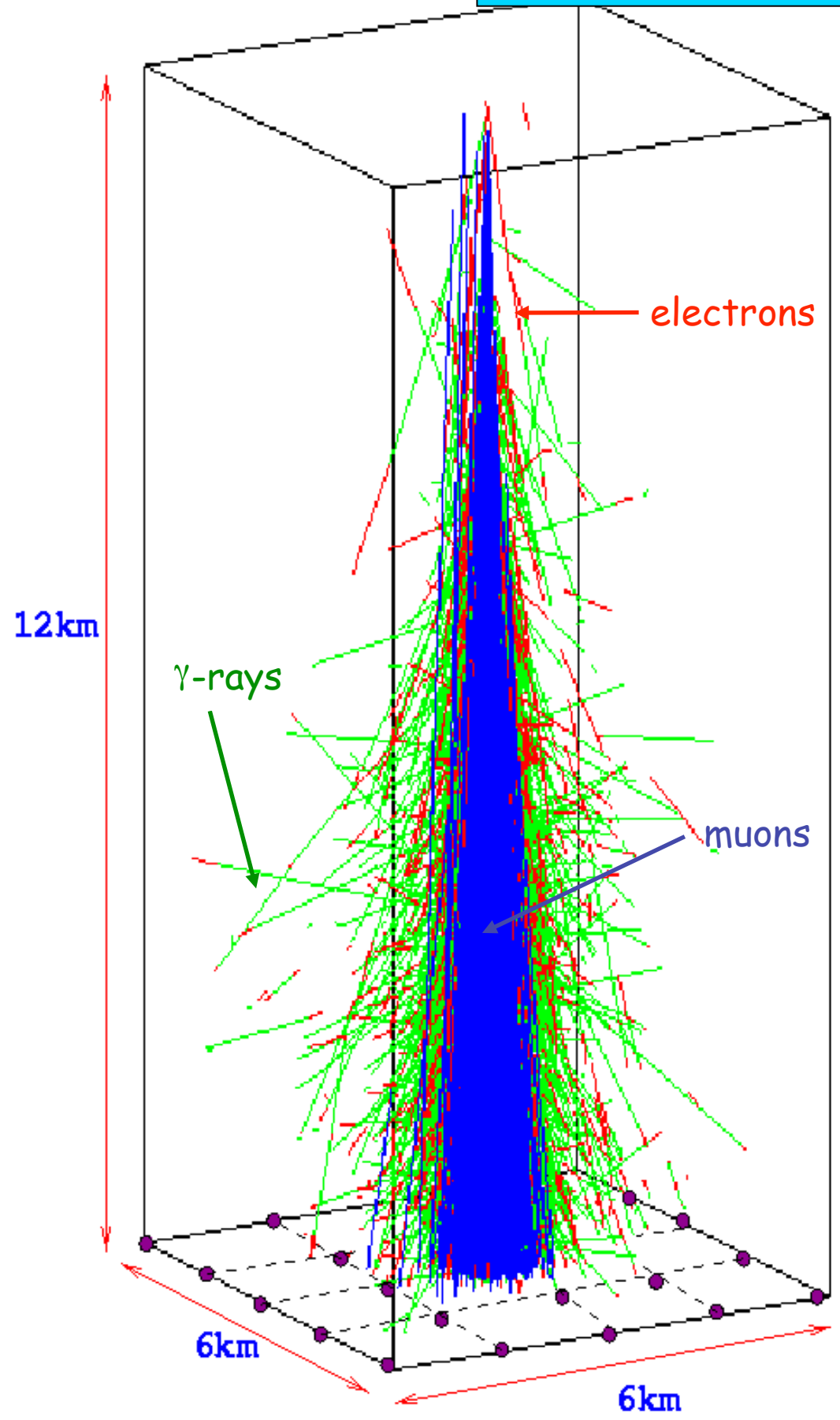
A. Coleman et al., *Cosmic and Energy Frontiers, Astropart. Phys.* 147 (2023) 102794

Fig. 9. Recent measurements of the all-particle flux from the TA [109], IceCube [81], Pierre Auger [33,48,67], Yakutsk [110], KASCADE-Grande [111], and TUNKA [112] experiments, which define the spectral features in the UHE region, are shown. Those with upgrades specifically described in this white paper are shown in color. The direction and magnitude of the systematic uncertainty in the energy scale for Auger and TA is indicated by the corresponding arrows.



Pierre Auger collaboration, V. Nowotny, ICRC 2021

Atmospheric Showers and their Detection

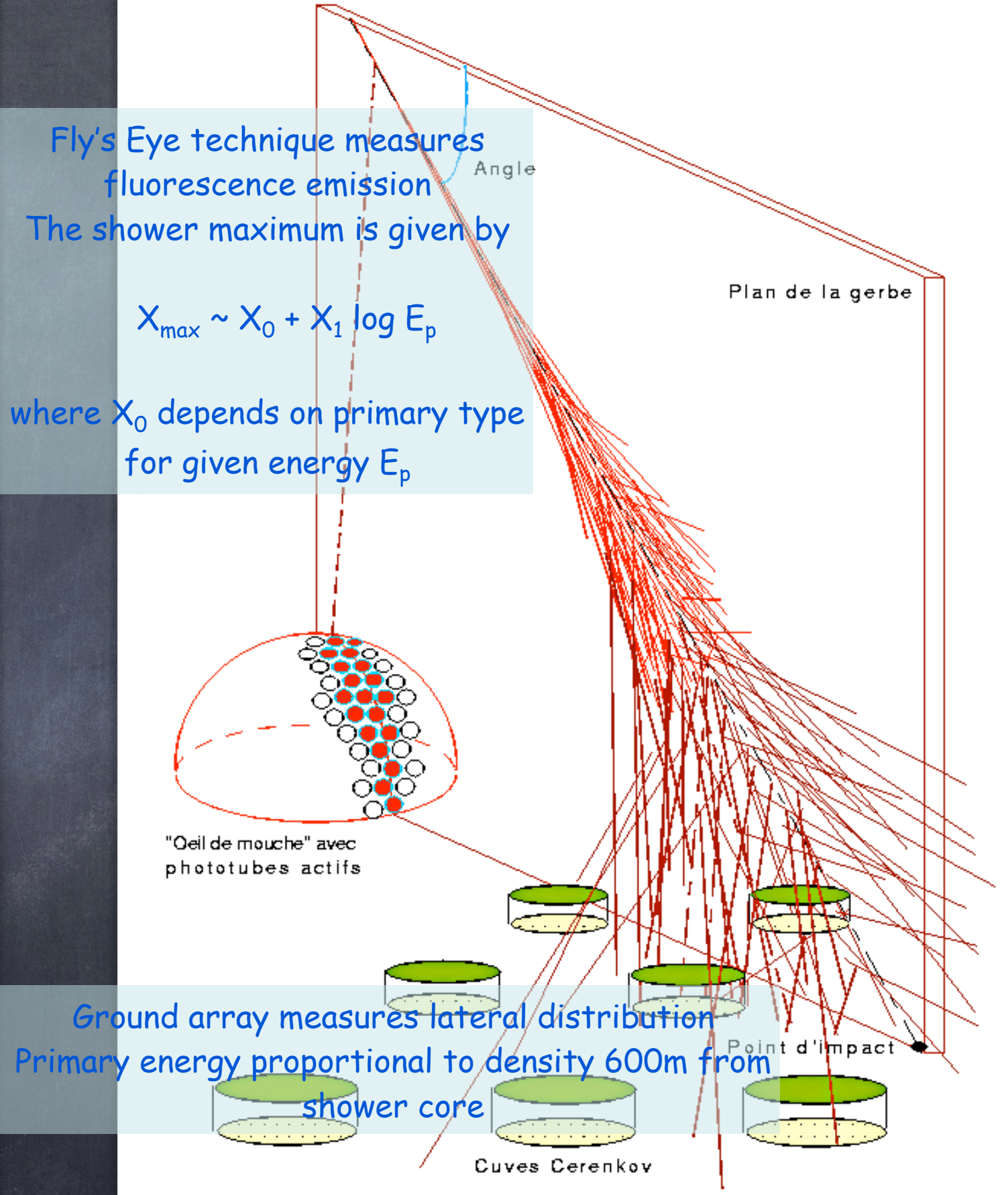


Fly's Eye technique measures fluorescence emission

The shower maximum is given by

$$X_{max} \sim X_0 + X_1 \log E_p$$

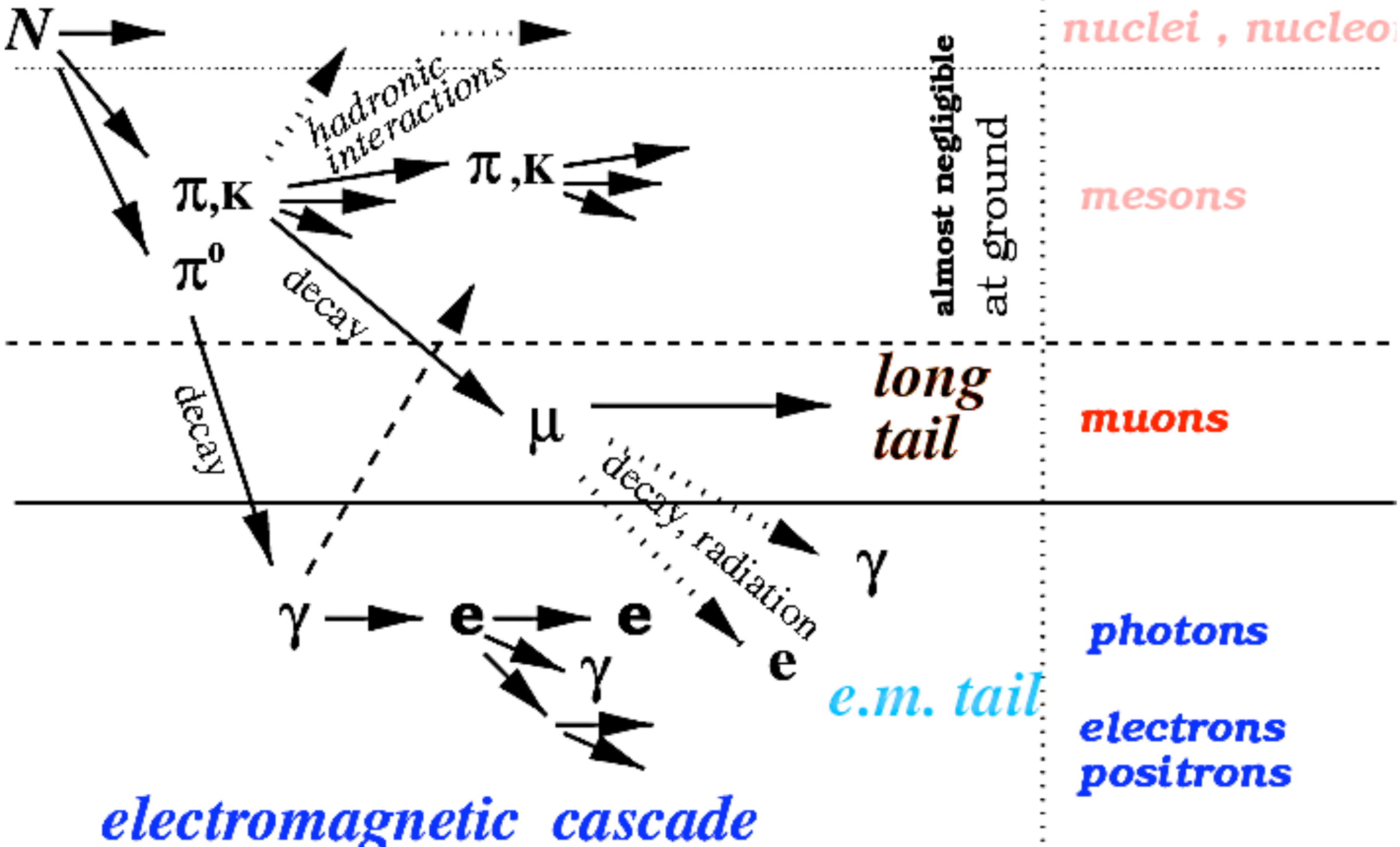
where X_0 depends on primary type for given energy E_p



Ground array measures lateral distribution

Primary energy proportional to density 600m from shower core

hadronic cascade



Some Air Shower Physics

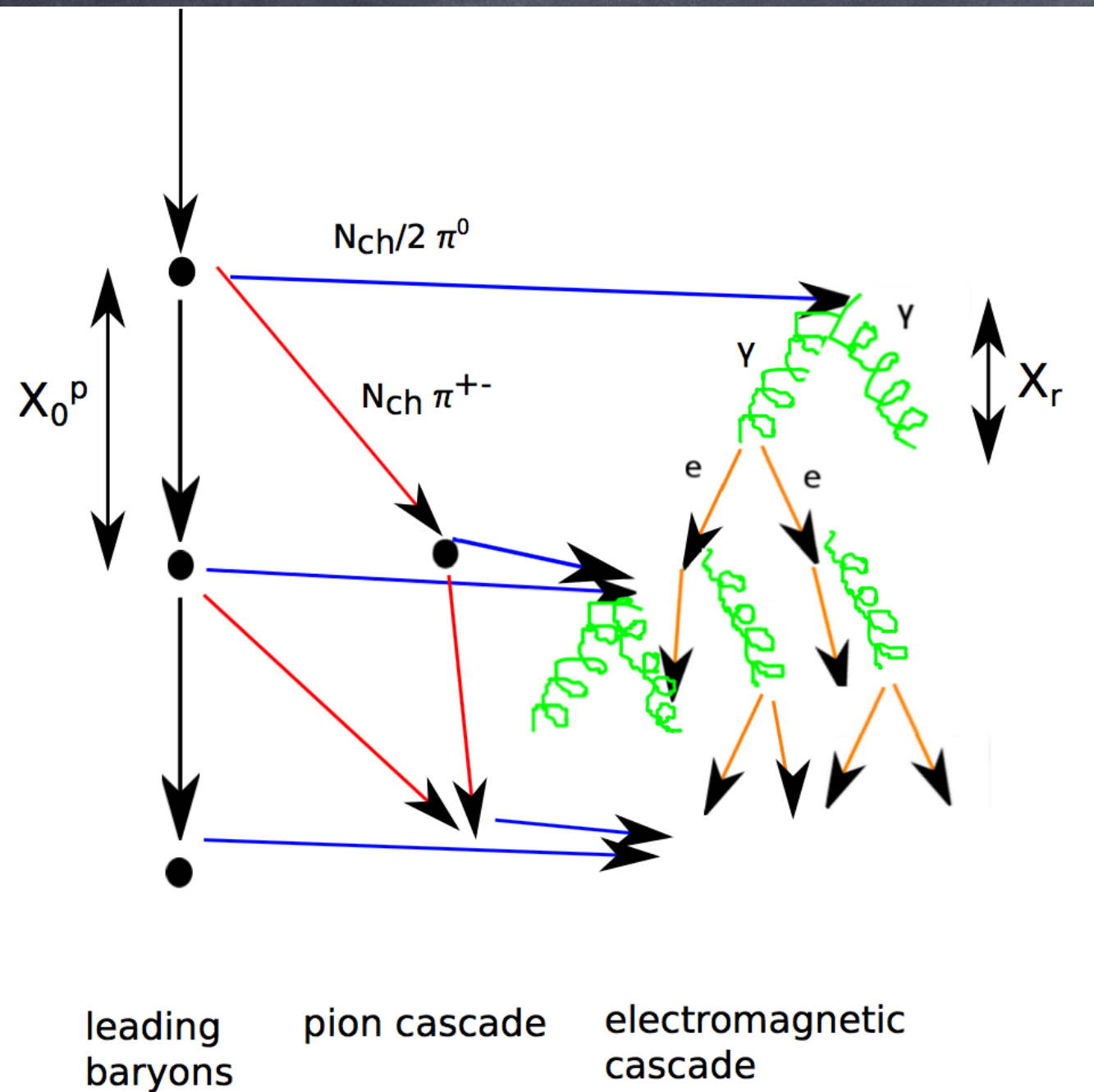


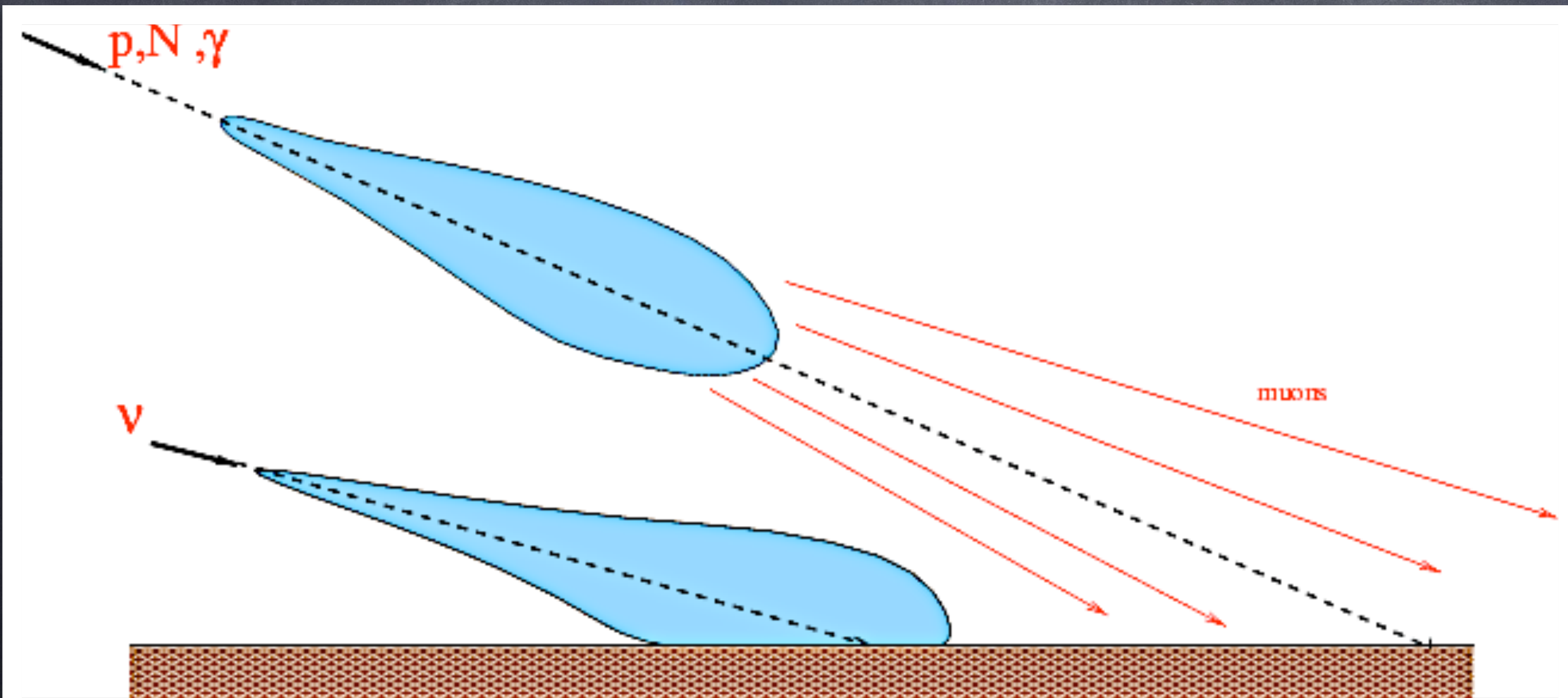
Fig. 5.2 A sketch of the first two generations of an hadronic cascade in the Heitler Matthews model [232] (left part) and of the first few generations of the electromagnetic cascade in the Heitler model [229] (right part). After each hadronic interaction length $X_0^p(E)$ the *leading baryon* produces $N_{ch}(E)$ charged pions and $N_{ch}(E)/2$ neutral pions. Neutral pions decay into two γ -rays instantaneously whereas charged pions interact again after column depth $\simeq X_0^p(E)$, producing further pions. High energy γ -rays produce electron-positron pairs after one radiation length X_r which in turn recreate γ -rays by bremsstrahlung after a similar length scale.

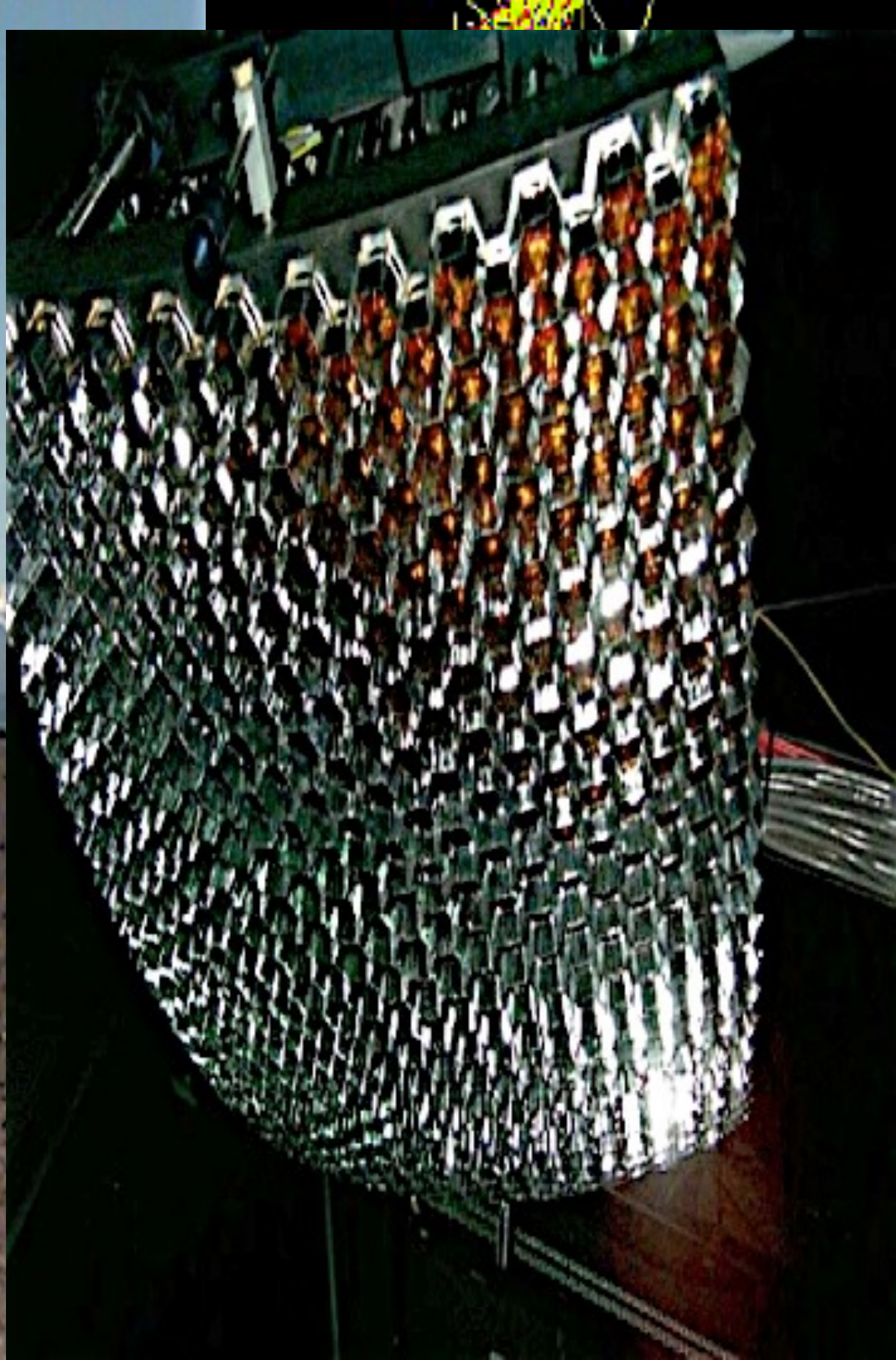
In this simple picture for a primary energy E_p the depth of shower maximum is the depth of first interaction X_0 plus the radiation length X_r times the number of generations n ,

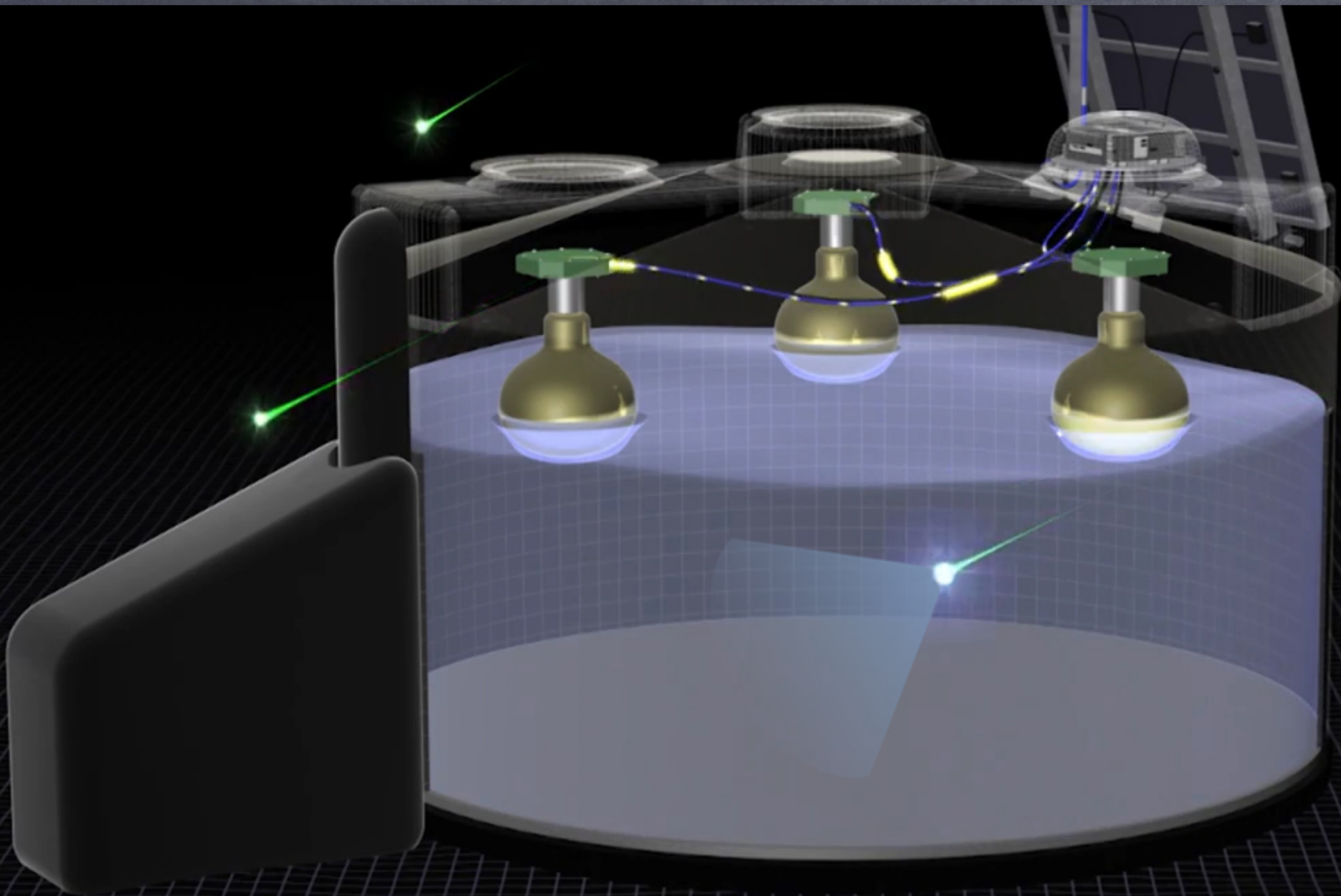
$$X_{\max} \sim X_0 + X_r \log (E_p/E_c)$$

where E_c is some critical energy

Cosmic ray versus neutrino induced air showers









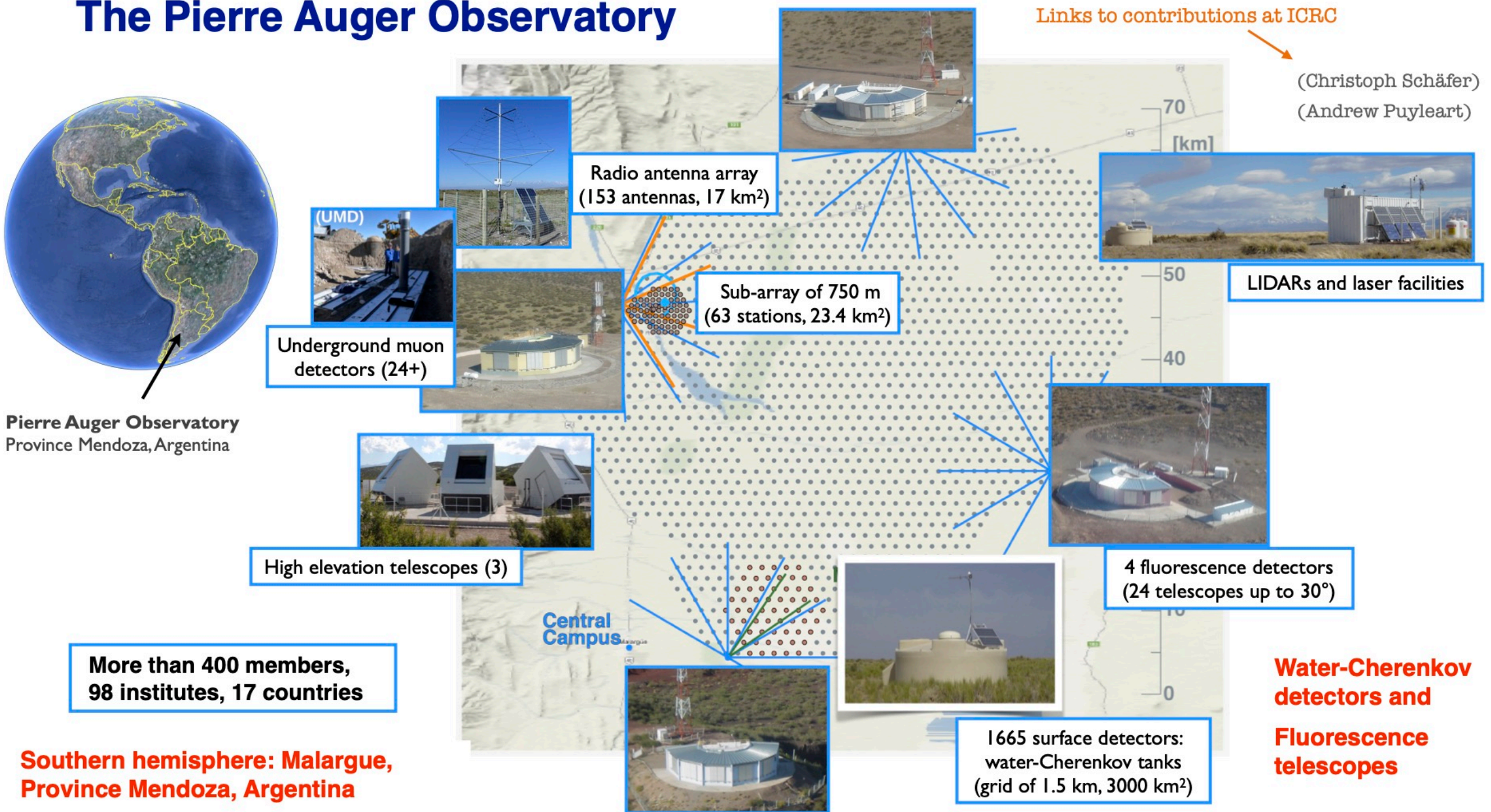
The Pierre Auger Observatory



Pierre Auger Observatory
Province Mendoza, Argentina

Links to contributions at ICRC

(Christoph Schäfer)
(Andrew Puyleart)

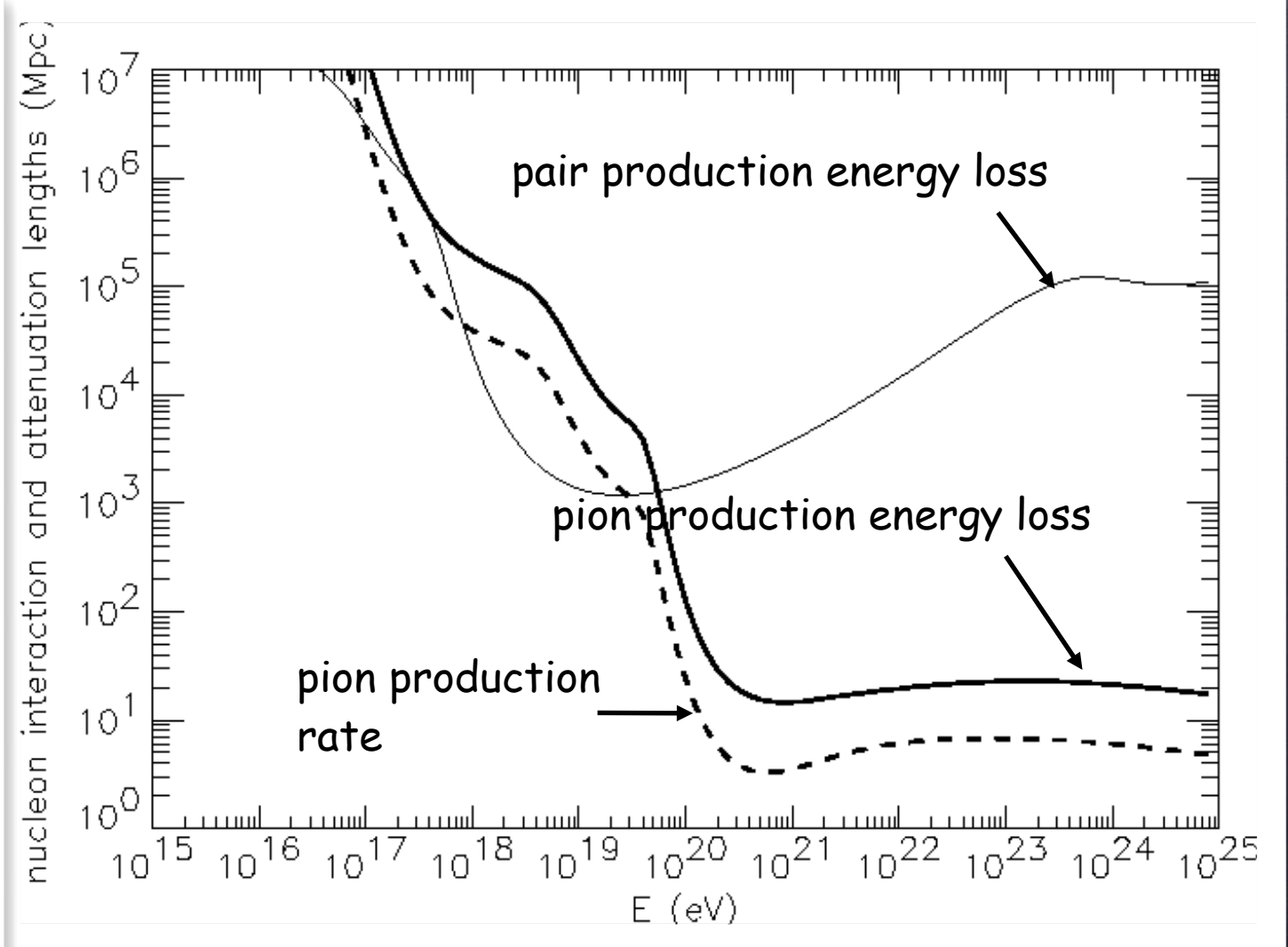
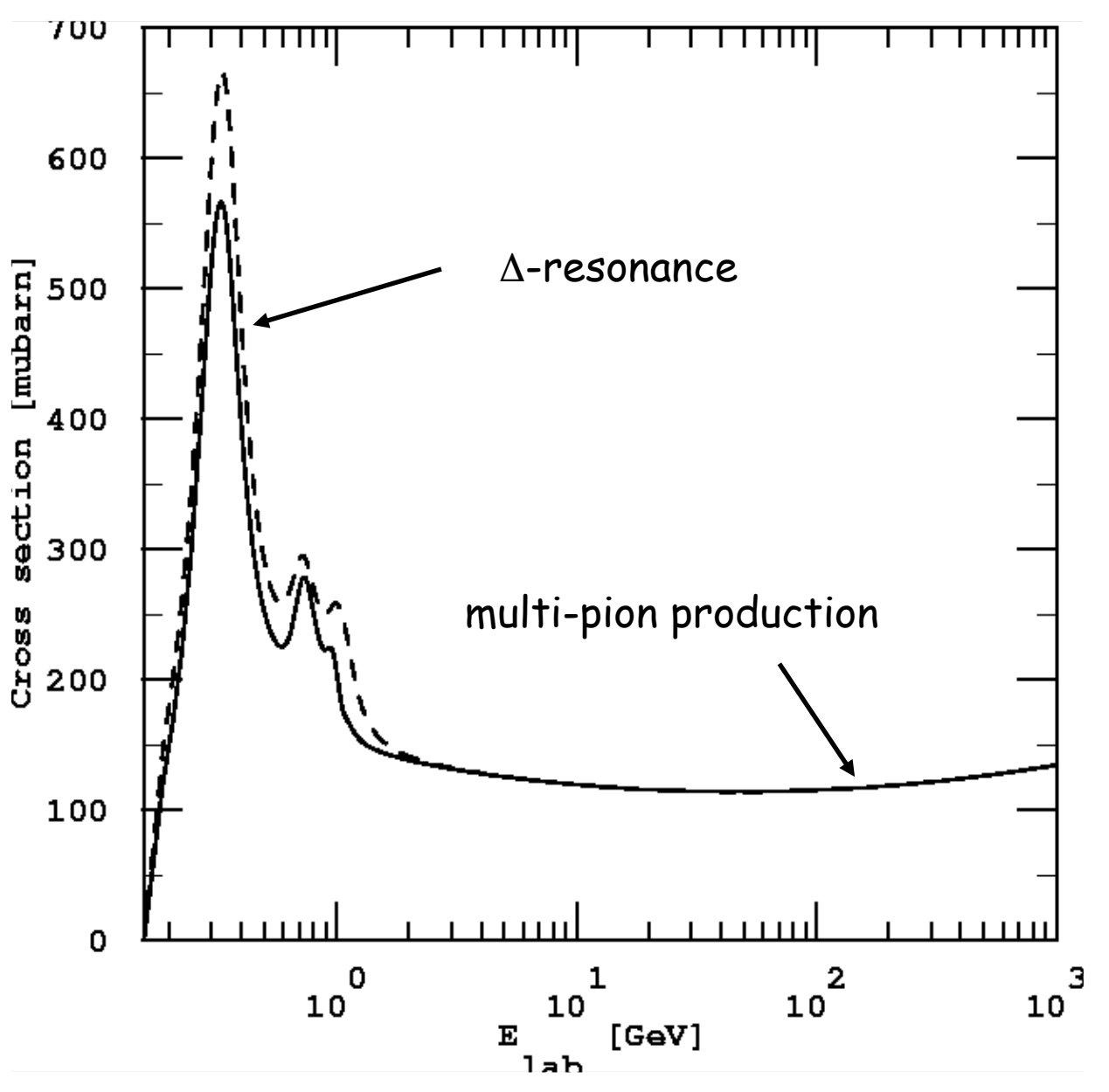
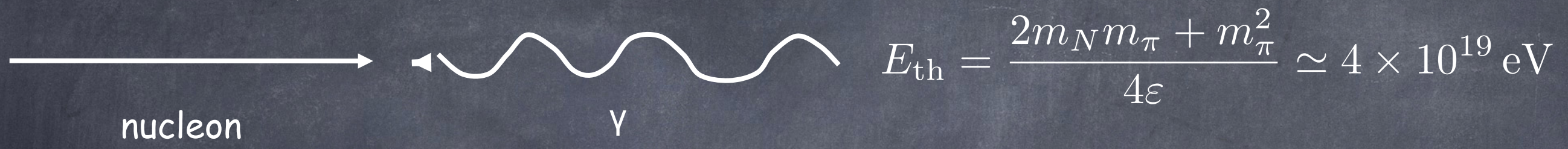


More than 400 members,
98 institutes, 17 countries

Southern hemisphere: Malargue,
Province Mendoza, Argentina

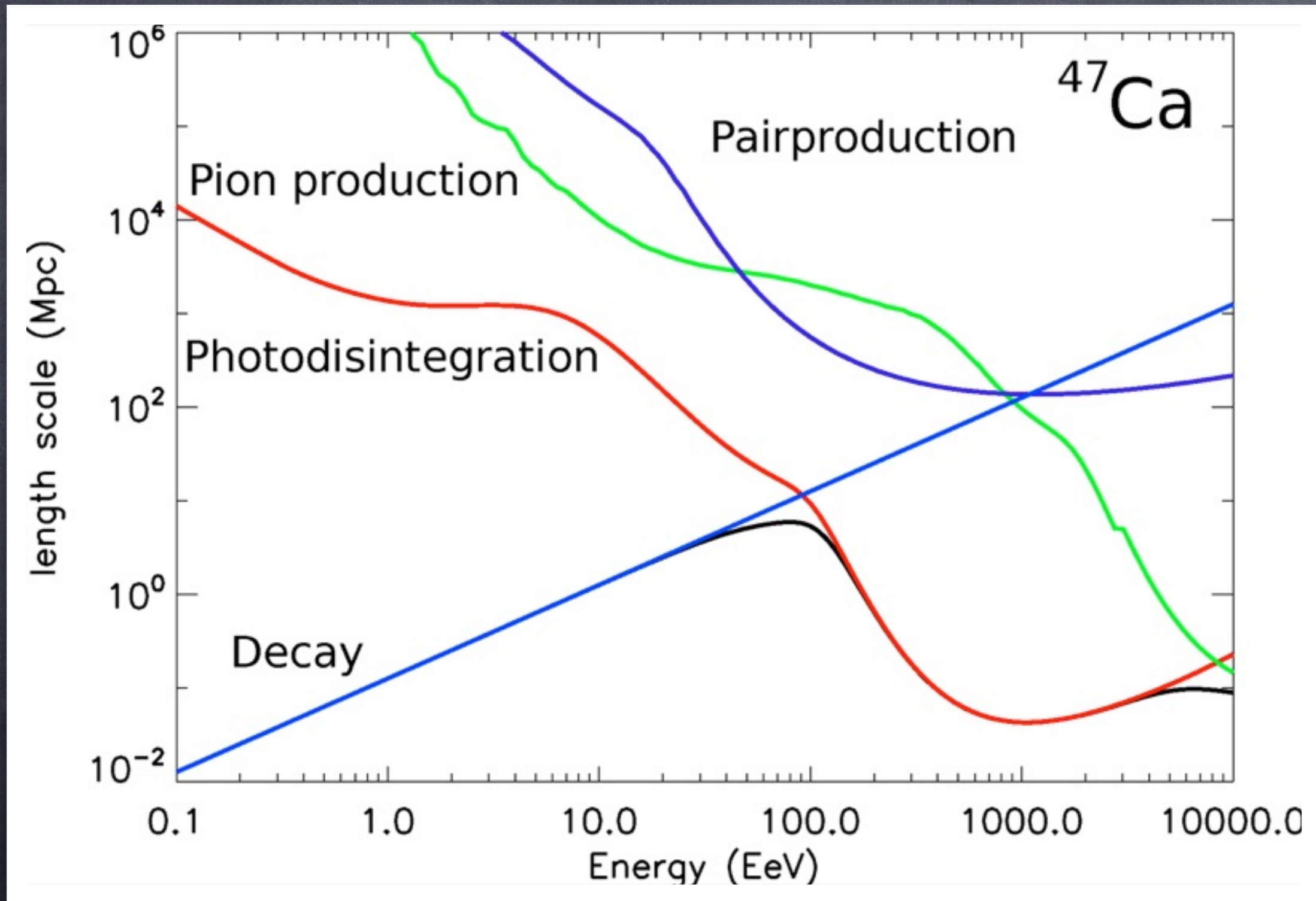
The Greisen-Zatsepin-Kuzmin (GZK) effect

Nucleons can produce pions on the cosmic microwave background

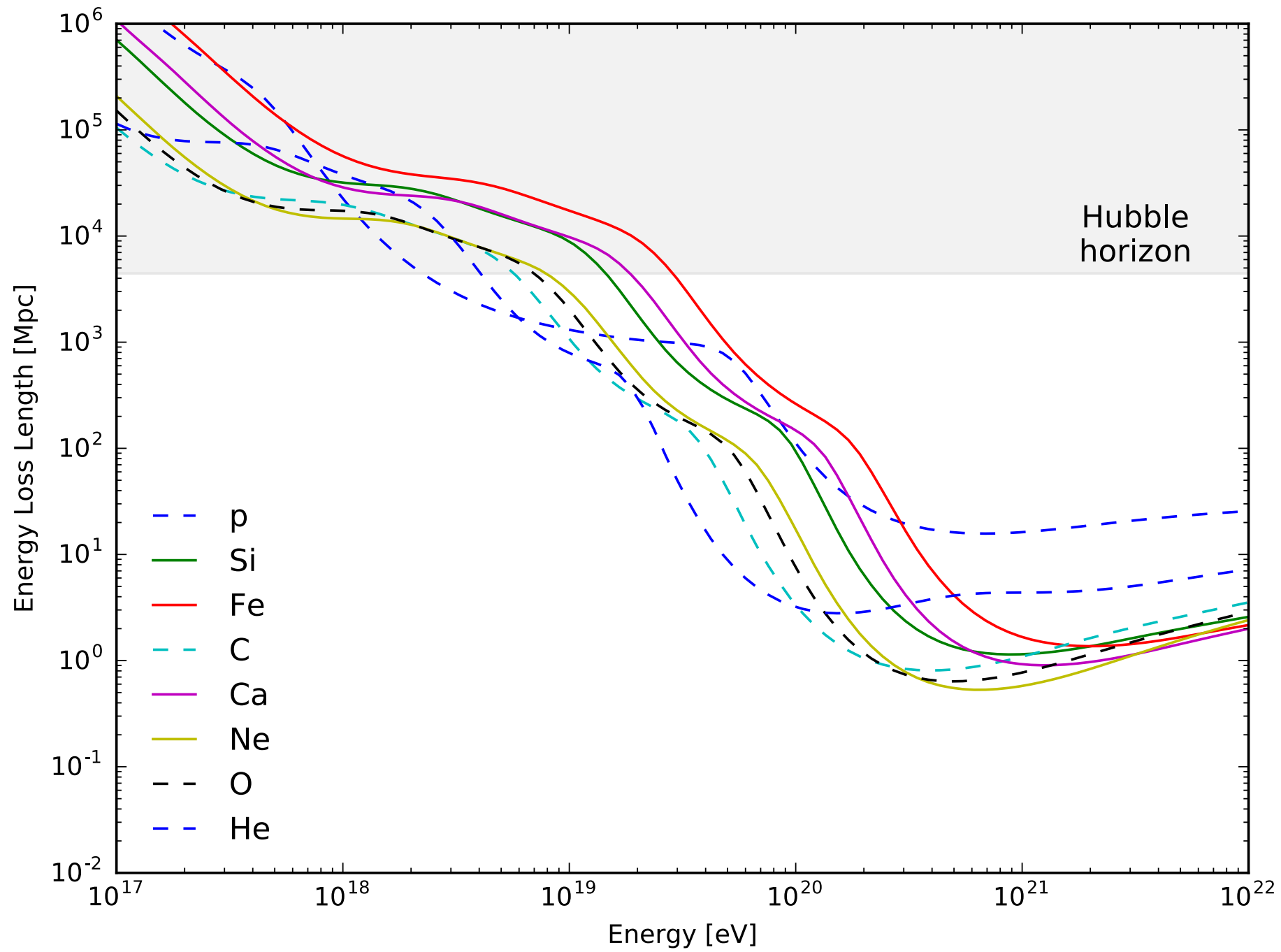


sources must be in cosmological backyard
 Only Lorentz symmetry breaking at $\Gamma > 10^{11}$
 could avoid this conclusion.

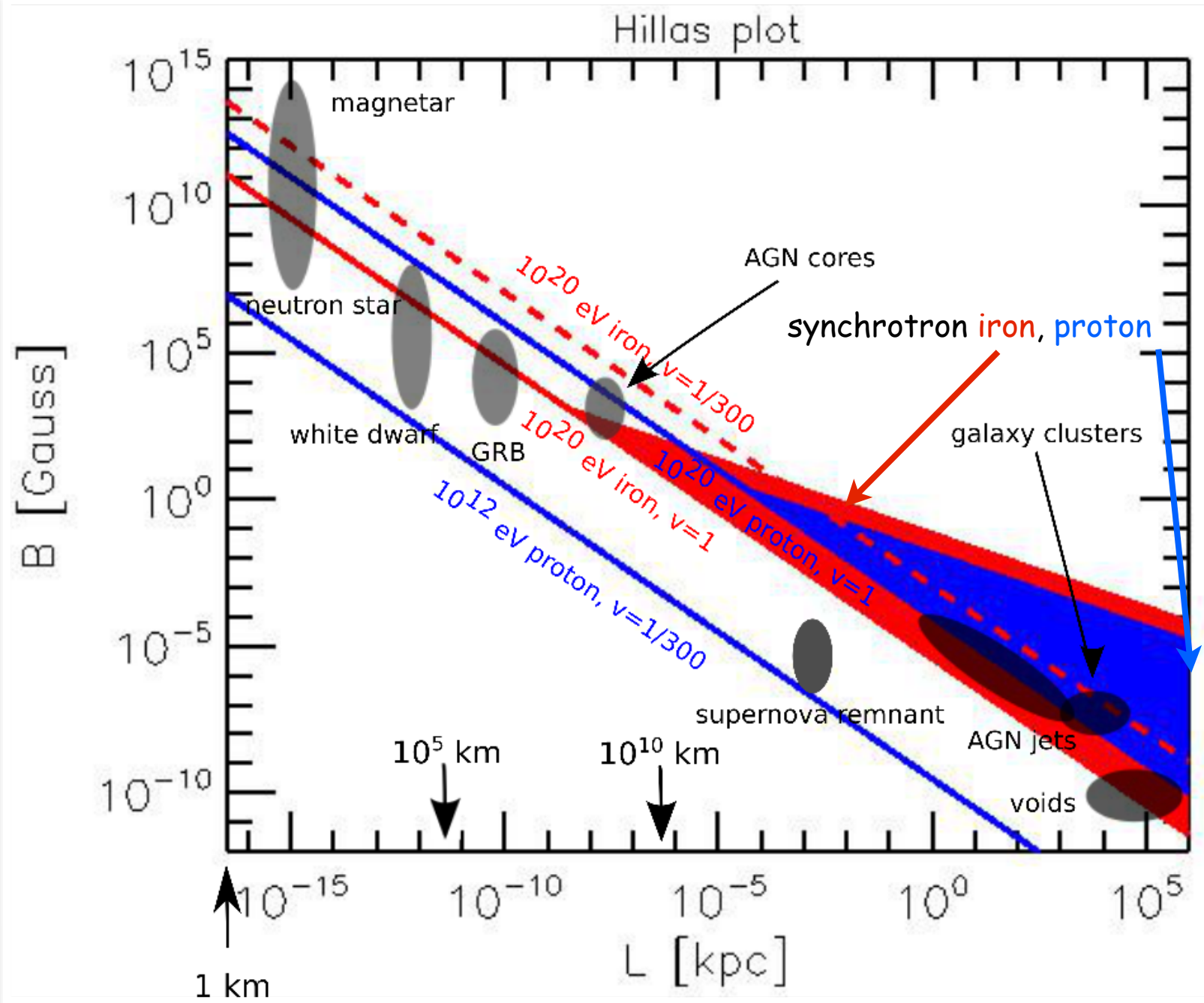
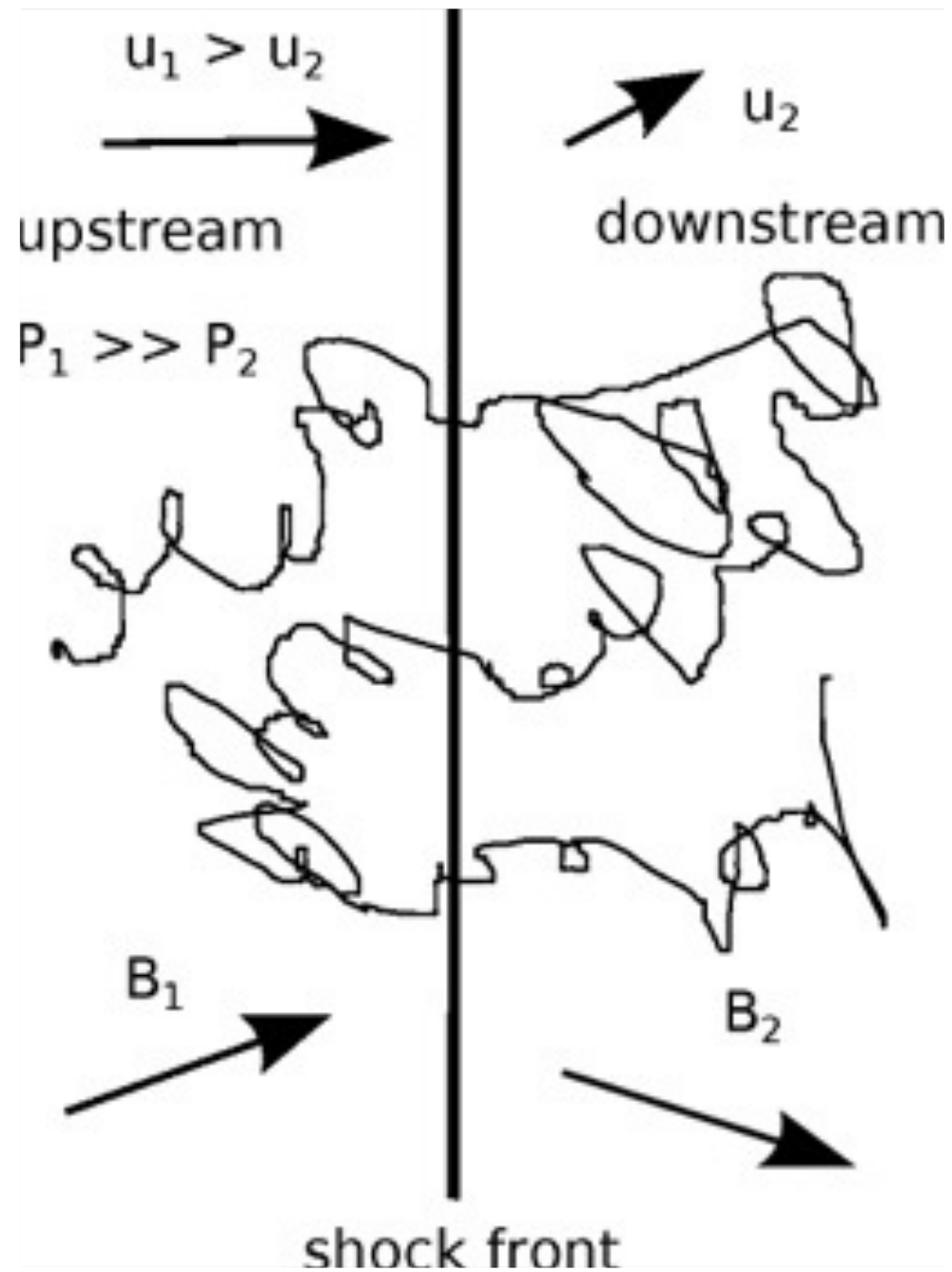
Length scales for relevant processes of a typical heavy nucleus



Energy Loss Lengths based on CRPropa



1st Order Fermi Shock Acceleration

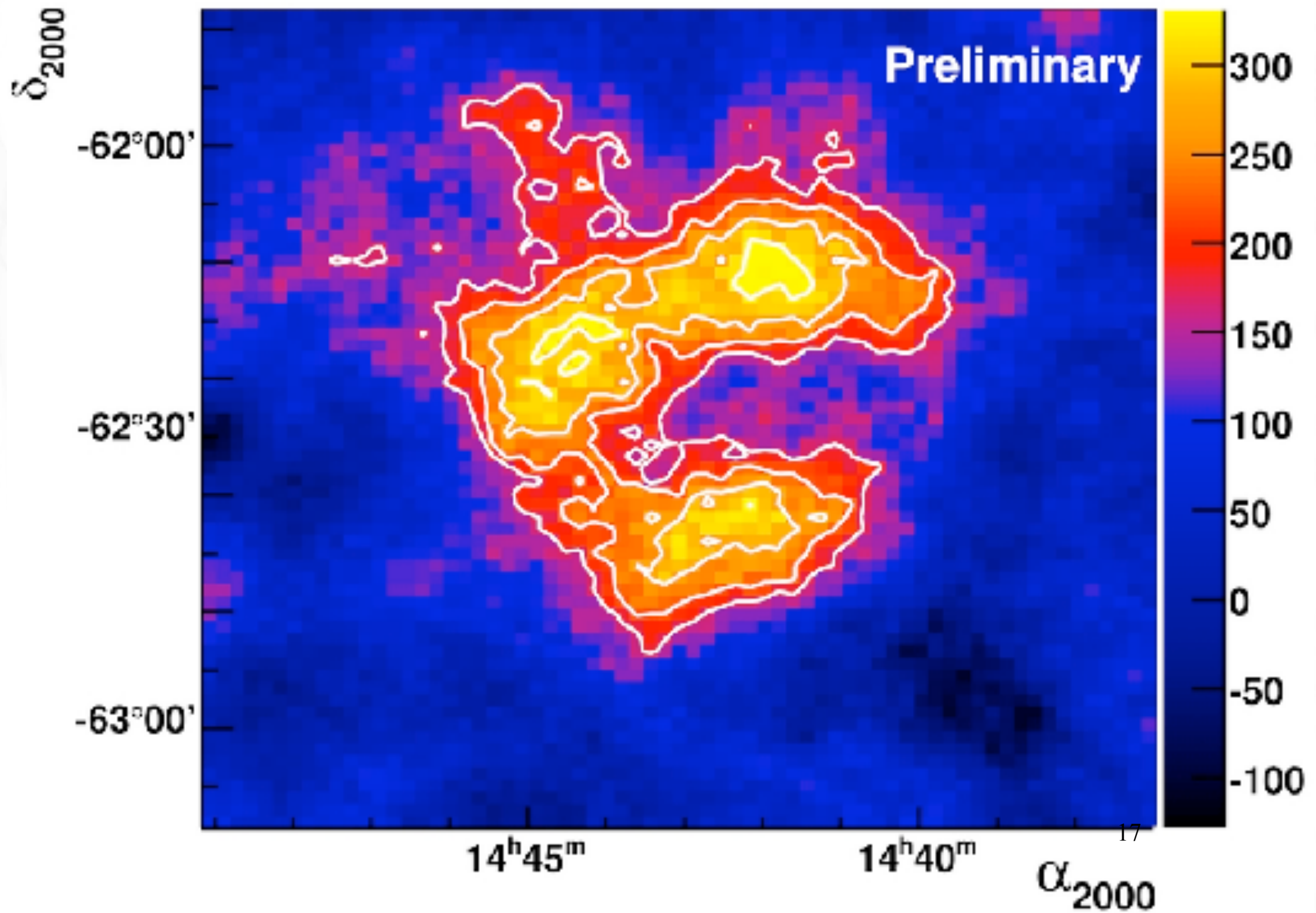


Fractional energy gain per shock crossing $\sim u_1 - u_2$ on a time scale r_L/u_2 .

Together with downstream losses this leads to a spectrum E^{-q} with $q > 2$ typically.

Confinement, gyroradius $<$ shock size, and energy loss times define maximal energy

Shell-type supernova remnant RCW 86 seen by HESS



Some general Requirements for Sources

Accelerating particles of charge eZ to energy E_{\max} requires induction $\epsilon > E_{\max}/eZ$. With $Z_0 \sim 100\Omega$ the vacuum impedance, this requires dissipation of minimum power of

$$L_{\min} \sim \frac{\epsilon^2}{Z_0} \simeq 10^{45} Z^{-2} \left(\frac{E_{\max}}{10^{20} \text{ eV}} \right)^2 \text{ erg s}^{-1}$$

This „Poynting“ luminosity can also be obtained from $L_{\min} \sim (BR)^2$ where BR is given by the „Hillas criterium“:

$$BR > 3 \times 10^{17} \Gamma^{-1} \left(\frac{E_{\max}/Z}{10^{20} \text{ eV}} \right) \text{ Gauss cm}$$

where Γ is a possible beaming factor.

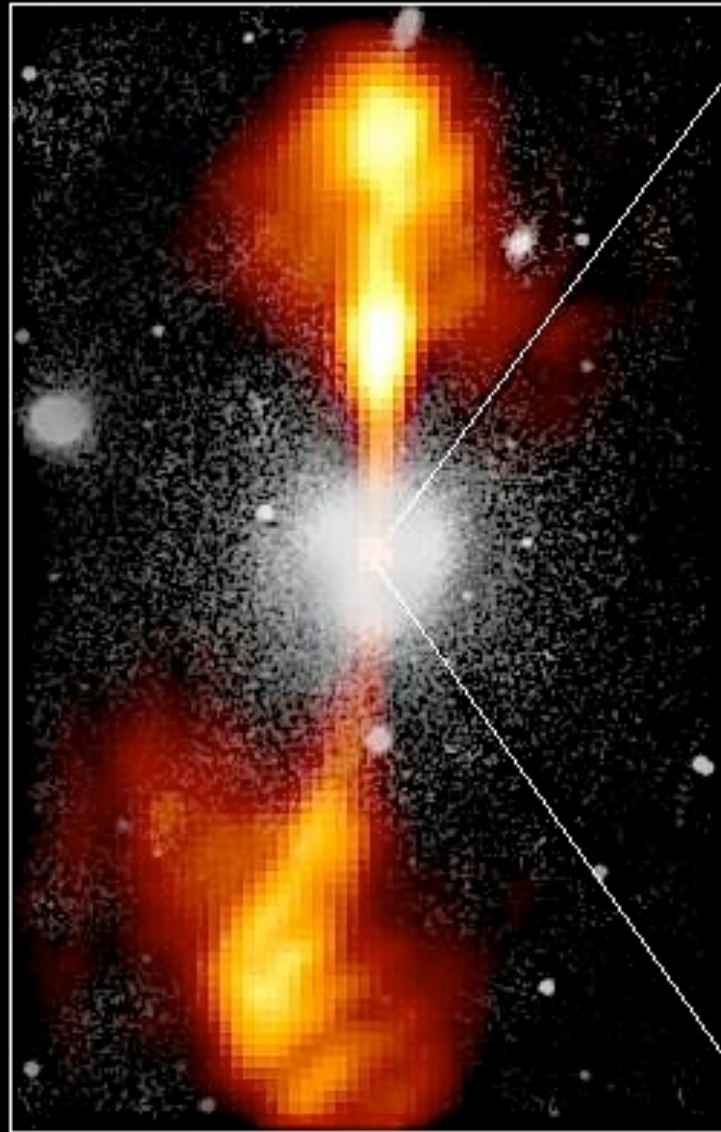
If most of this goes into electromagnetic channel, only AGNs and maybe gamma-ray bursts could be consistent with this.

A possible acceleration site associated with shocks in hot spots of active galaxies

Core of Galaxy NGC 4261

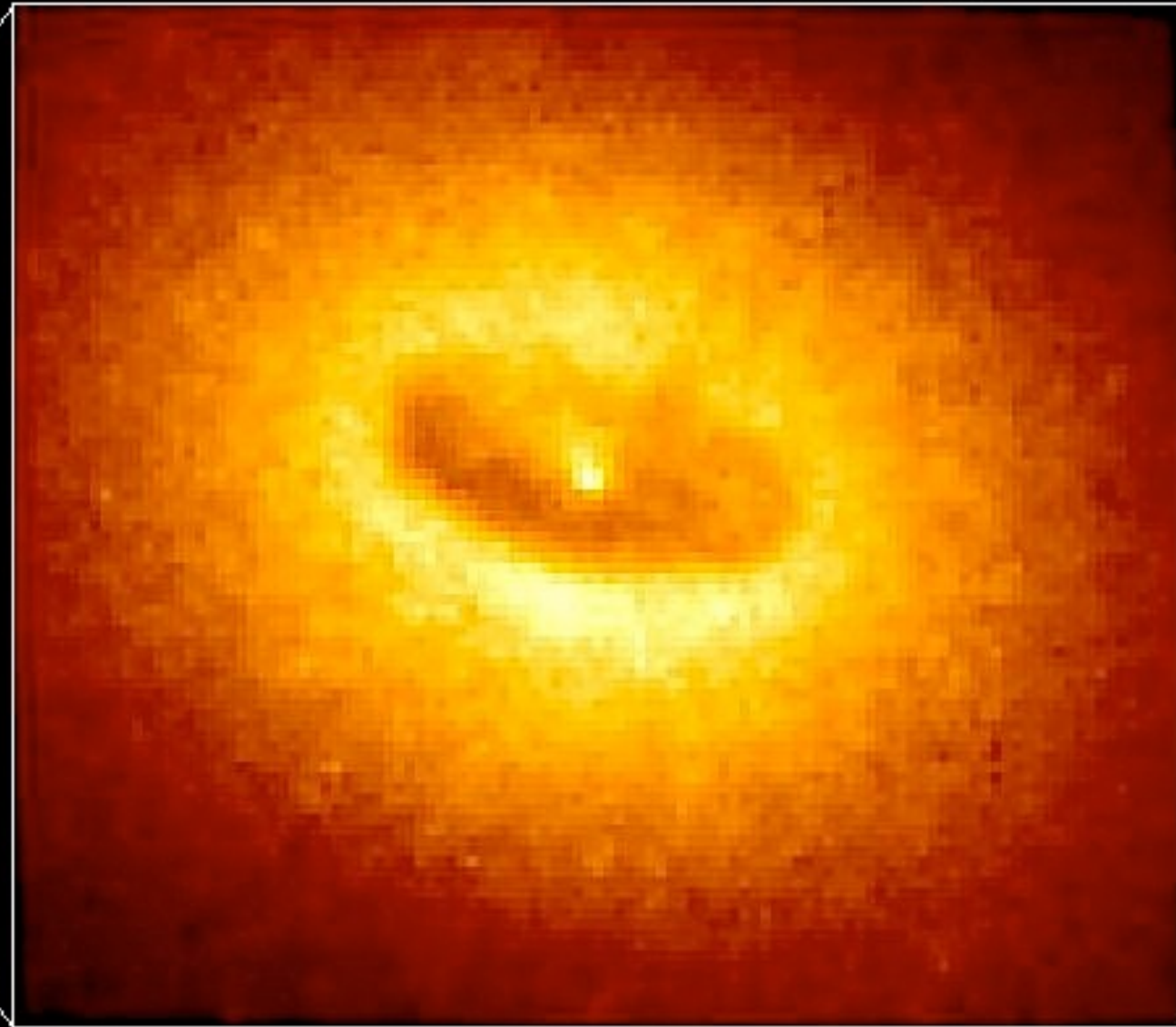
Hubble Space Telescope
Wide Field / Planetary Camera

Ground-Based Optical/Radio Image



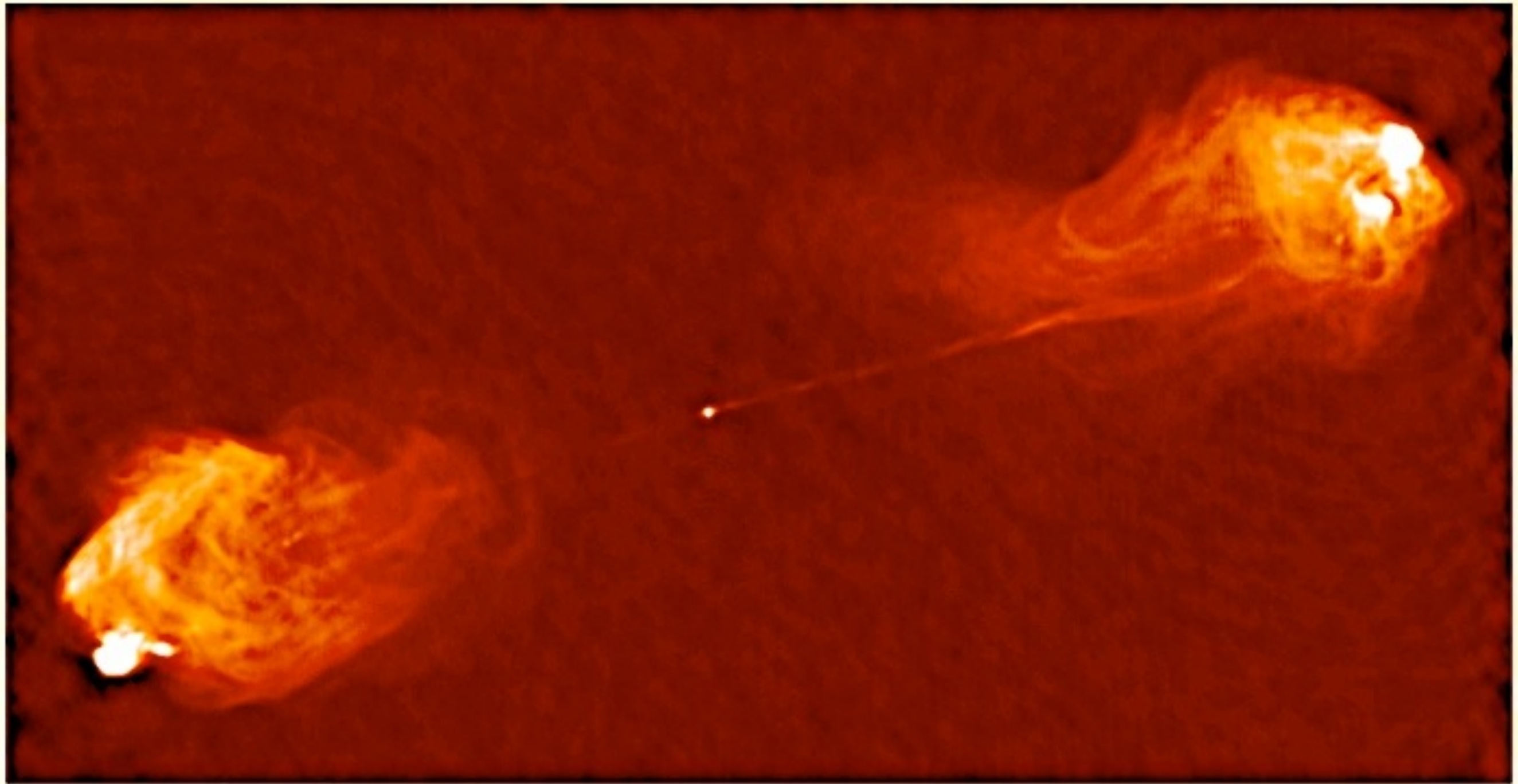
380 Arc Seconds
88,000 LIGHTYEARS

HST Image of a Gas and Dust Disk



17 Arc Seconds
400 LIGHTYEARS

Or Cygnus A



Mass Composition

Depth of shower maximum X_{\max} and its distribution contain information on primary mass composition

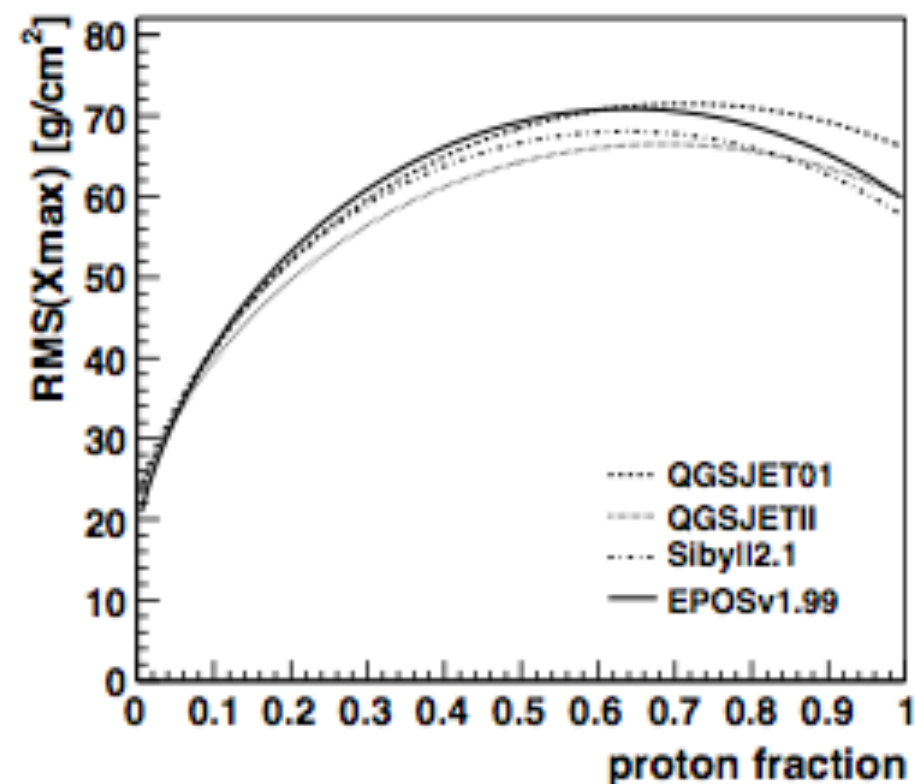
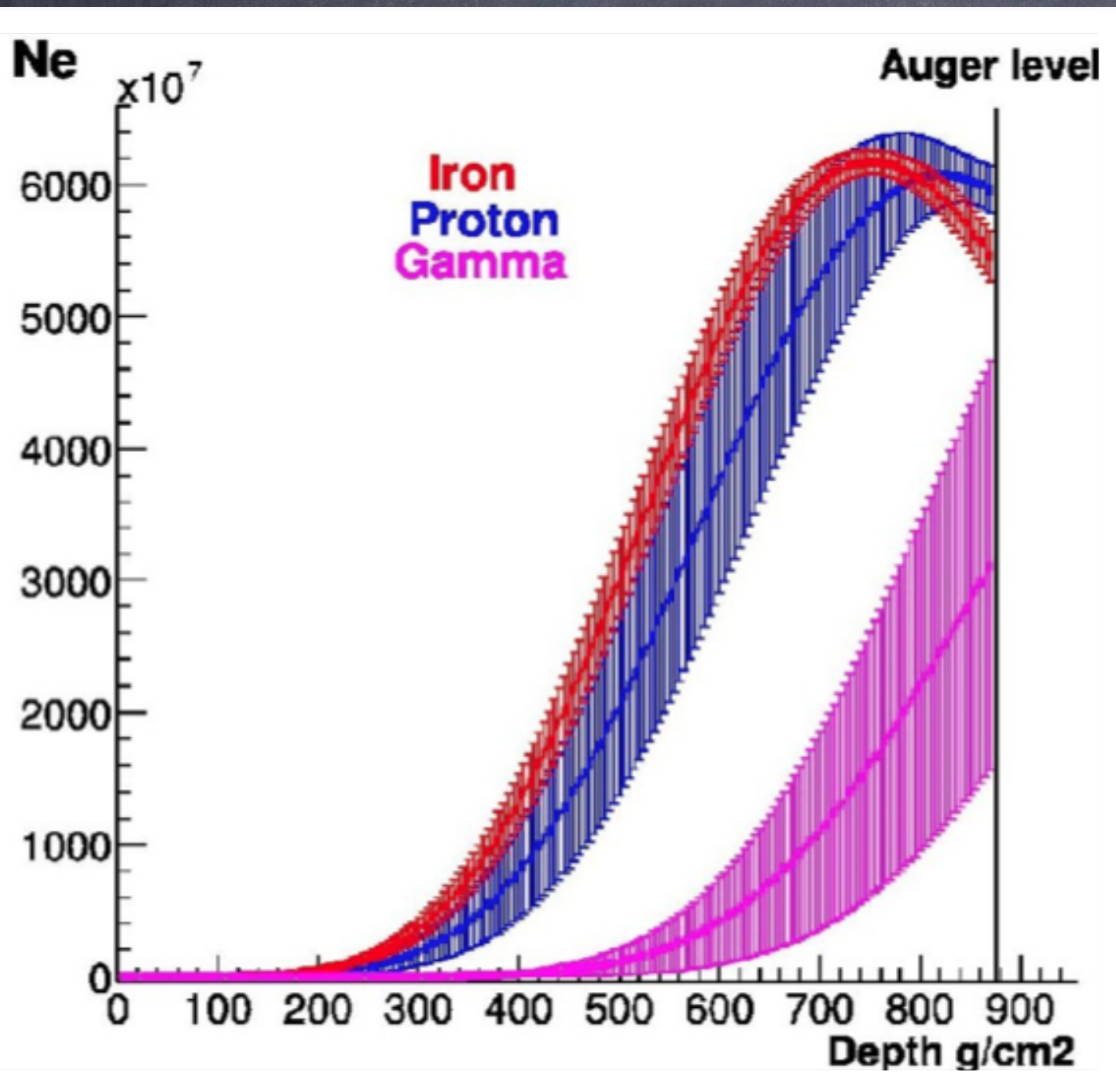
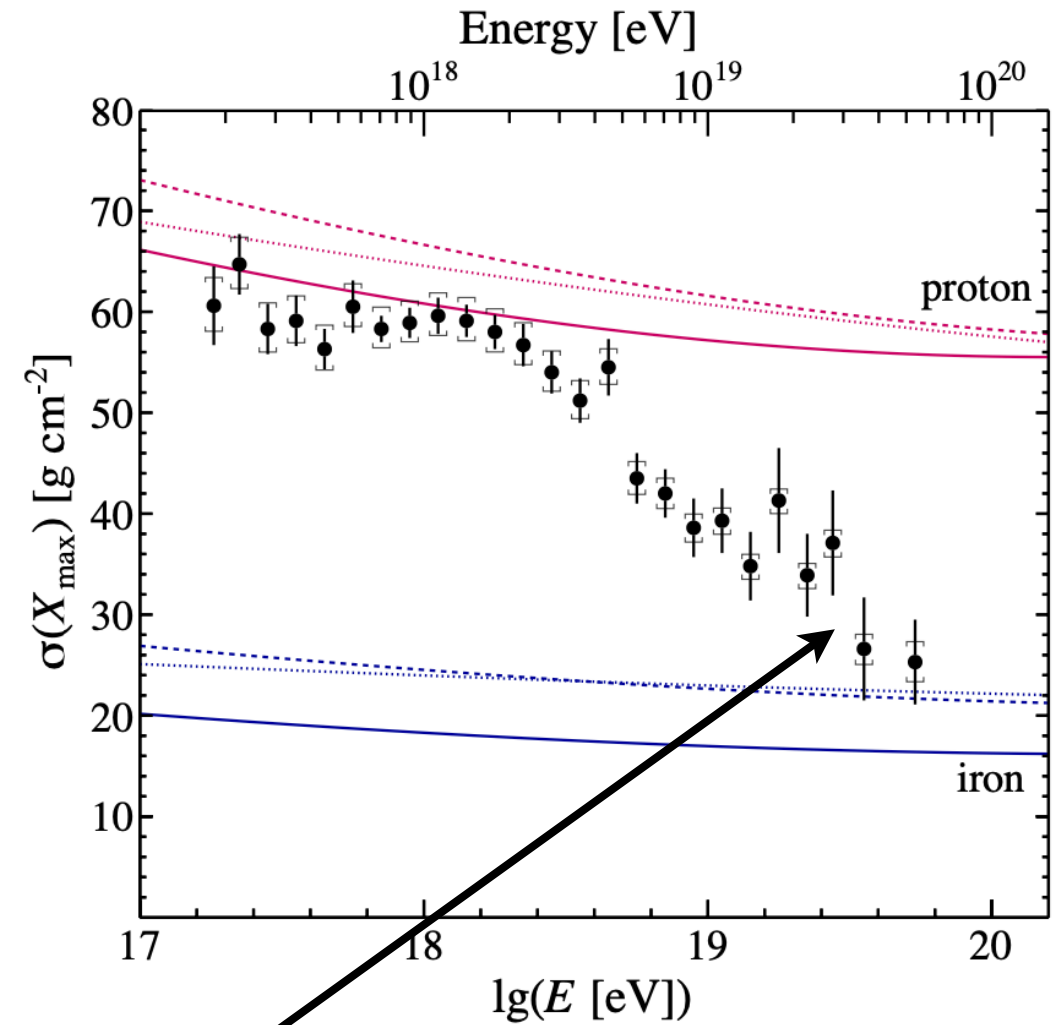
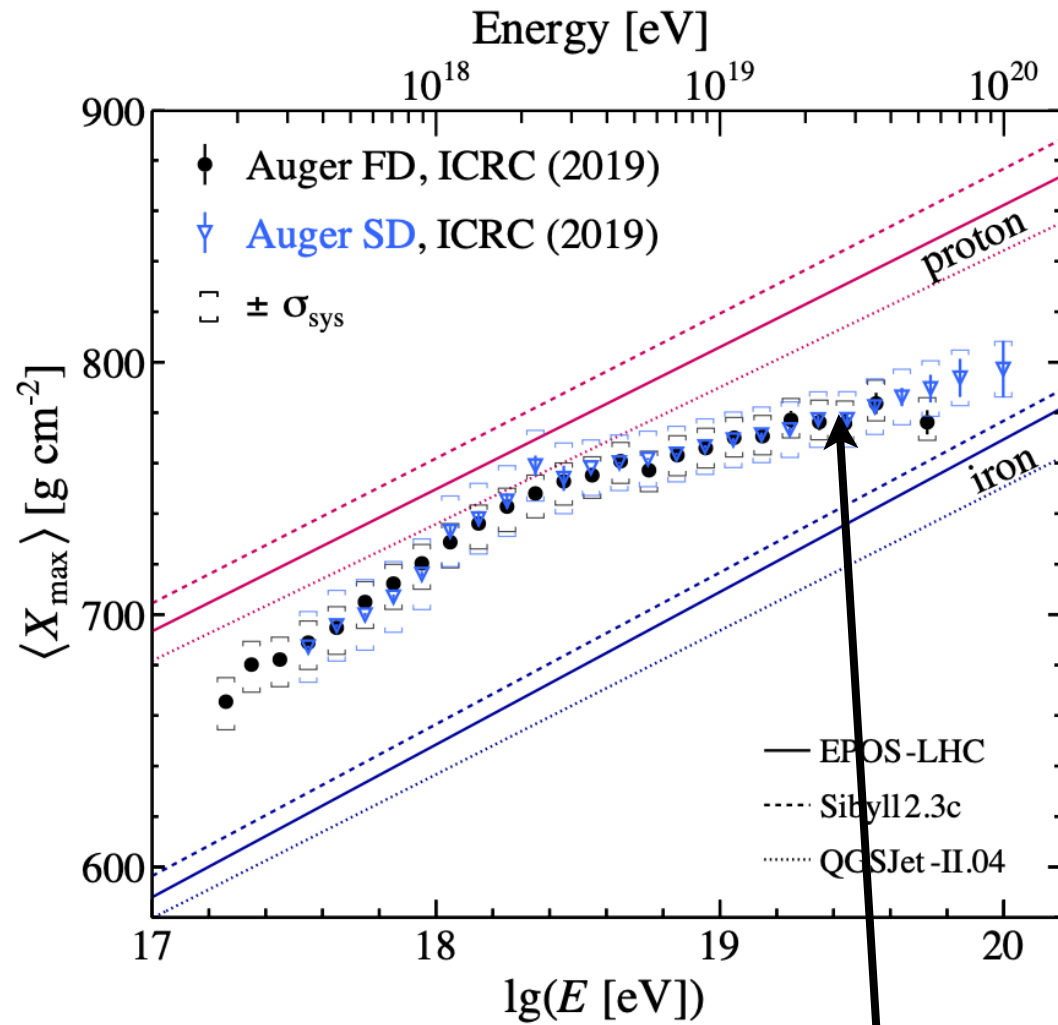


FIGURE 1. $RMS(X_{\max})$ from different hadronic interaction models [23] and a two-component p/Fe composition model ($E = 10^{18}$ eV).

Pierre Auger data suggest a heavier composition toward highest energies:



taken from R. Engel, Pierre Auger highlights, ICRC 2021

Important: LHC-tuned interaction models used for interpretation

(Phys. Rev. D90 (2014), 122005 & 122005, updated ICRC 2019)

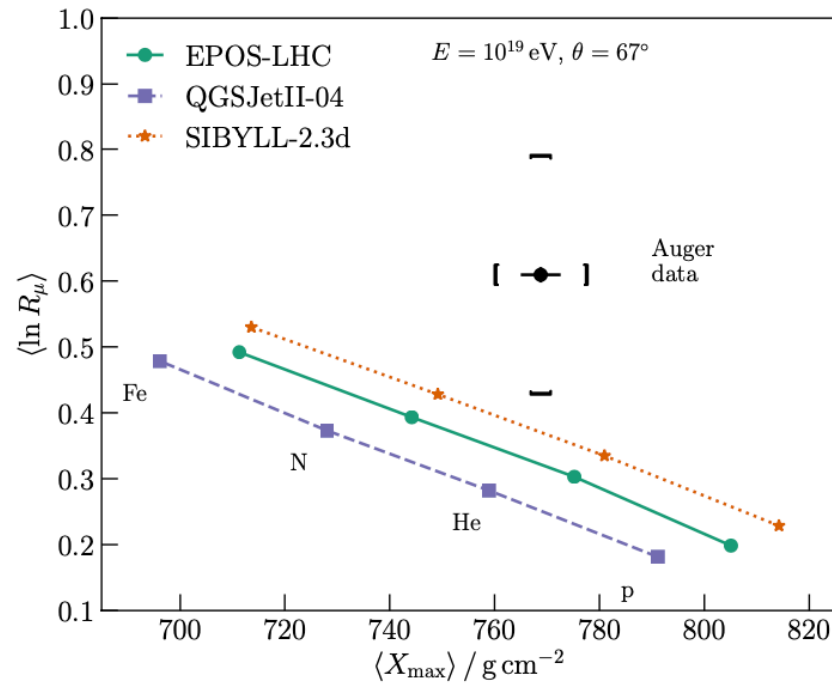
(Phys. Rev. D96 (2017), 122003)

potential tension with air shower simulations and some hadronic interaction models because a mixed composition would predict larger $RMS(X_{\max})$

within statistics consistent with the northern hemisphere observed by HiRes and Telescope Array

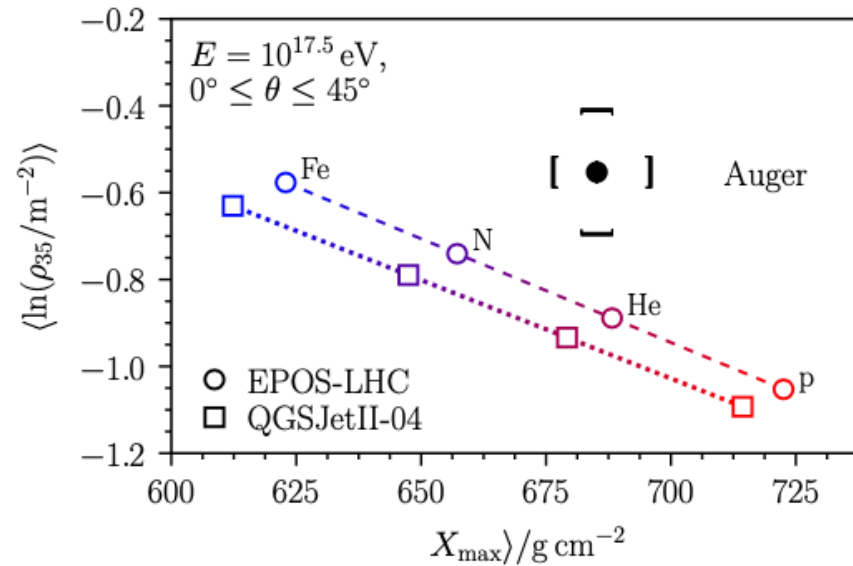
Muon number measured are systematically higher than predicted

Hybrid events and inclined showers

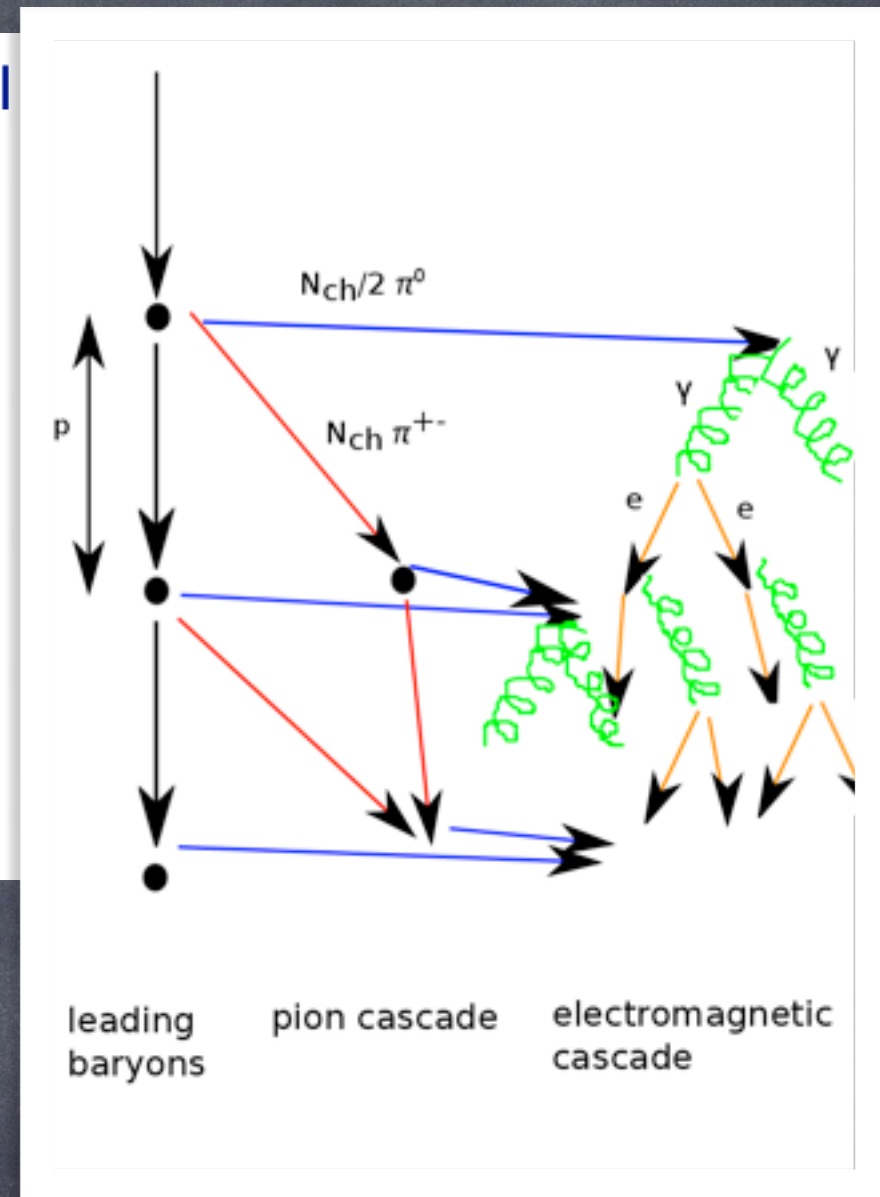


(Phys. Rev. Lett. 117 (2016) 192001,
Phys. Rev. D91 (2015) 032003)

Muon counters and vertical



(Eur. Phys. J. C80 (2020) 751)

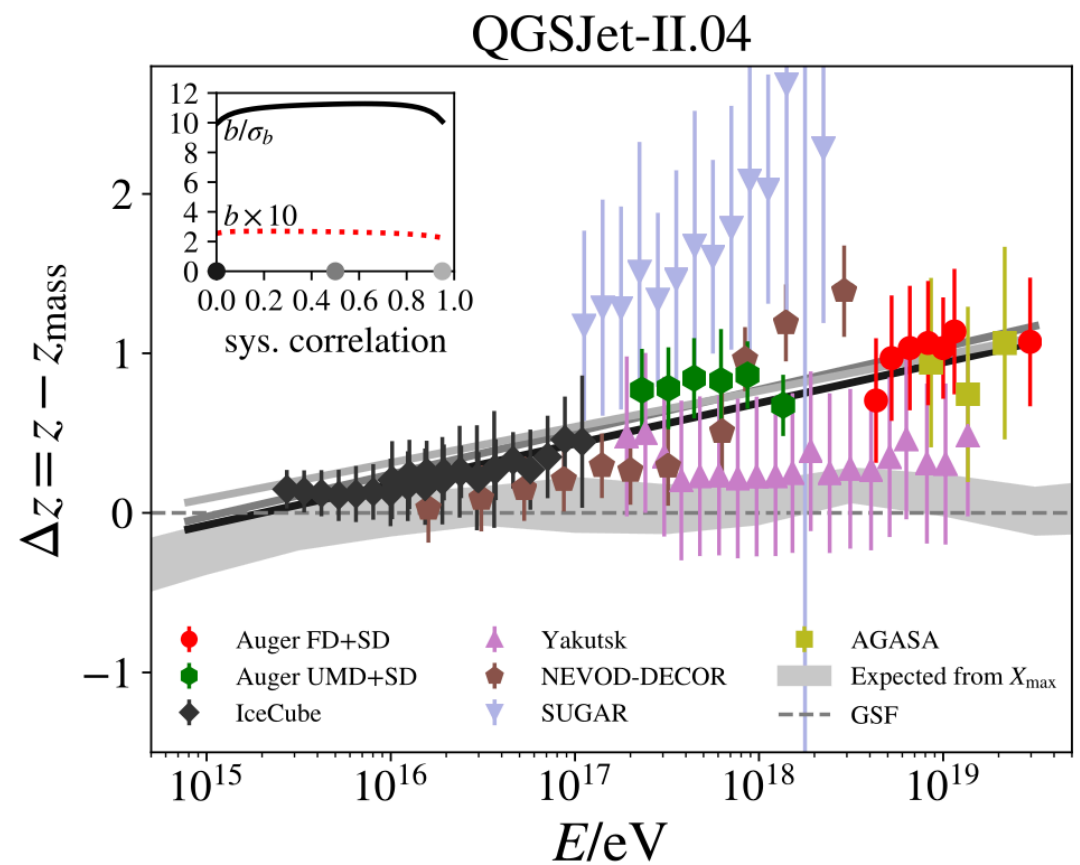
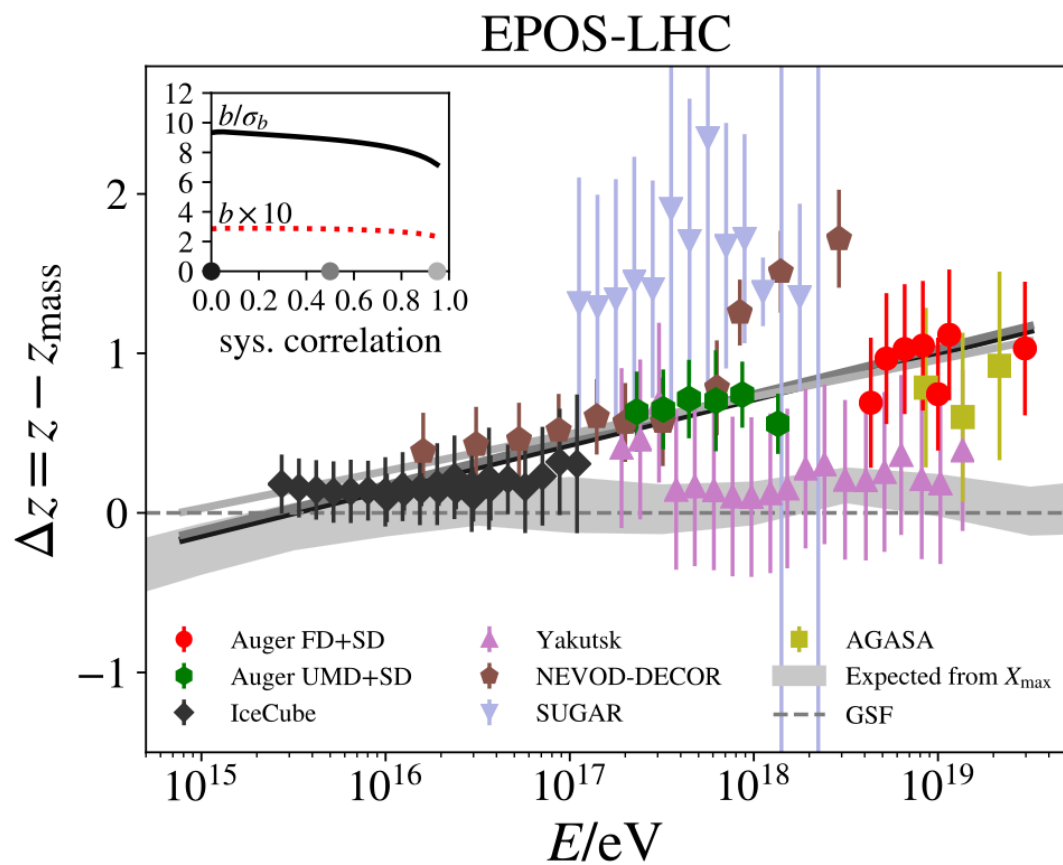


Pierre Auger Collaboration highlights, R. Engel, ICRC 2021

The muon number scales as

$$N_\mu \propto E_{\text{had}} \propto (1 - f_{\pi^0})^N,$$

with the fraction going into the electromagnetic channel $f_{\pi^0} \simeq \frac{1}{3}$ and the number of generations N strongly constrained by X_{\max} . Larger N_μ thus requires smaller f_{π^0} ! The production of ρ^0 could also play a role.

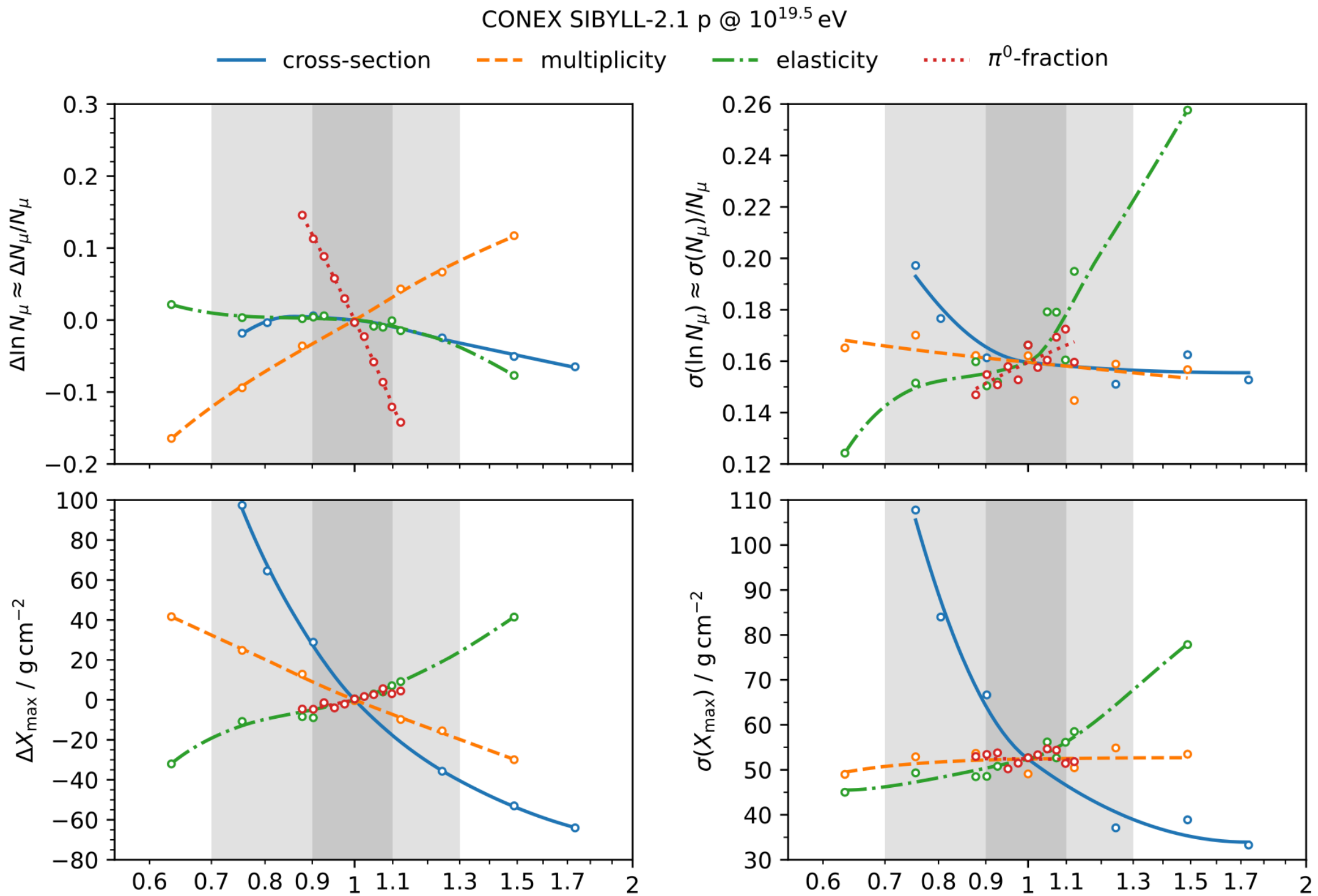


D. Soldin, arXiv:2302.07111, RICAP 2021

Figure 1. Linear fits of the form $\Delta z = a + b \cdot \log_{10}(E/10^{16} \text{ eV})$ to the $\Delta z = z - z_{\text{mass}}$ distributions, as described in Ref. [9]. Shown in the inset are the slope, b , and its deviation from zero in standard deviations for an assumed correlation of the uncertainties within each experiment (for details see Ref. [10]). Examples of the fits are shown for a correlation of 0.0, 0.5, and 0.95 in varying shades of gray.

$$\Delta z \equiv \frac{\ln \langle N_{\mu} \rangle - \ln \langle N_{\mu,p}^{\text{det}} \rangle}{\ln \langle N_{\mu,\text{Fe}}^{\text{det}} \rangle - \ln \langle N_{\mu,p}^{\text{det}} \rangle} - \frac{\langle \ln A \rangle}{56}$$

where N_{μ} is the measured muon number, $N_{\mu,i}^{\text{det}}$ is the muon number predicted to be detected for species i and $\langle \ln A \rangle$ is composition deduced from measured X_{max} . A consistent hadronic model would give $\Delta z = 0$ within the superposition approximation.



D. Soldin, arXiv:2302.07111, RICAP 2021

Figure 2. Impact of changing basic parameters of hadronic interactions at $\sqrt{s_{\text{NN}}} = 13 \text{ TeV}$ and extrapolating logarithmically (see Ref. [18] for details) on the means and standard deviations of the logarithm of the muon number N_μ (top row) and the depth X_{max} of the shower maximum (bottom row) for a $10^{19.5}$ eV proton shower simulated with SIBYLL 2.1 [1]. The shaded bands highlight a $\pm 10\%$ and $\pm 30\%$ modification. The figure is an update of the original data from Ref. [18], taken from Ref. [8].

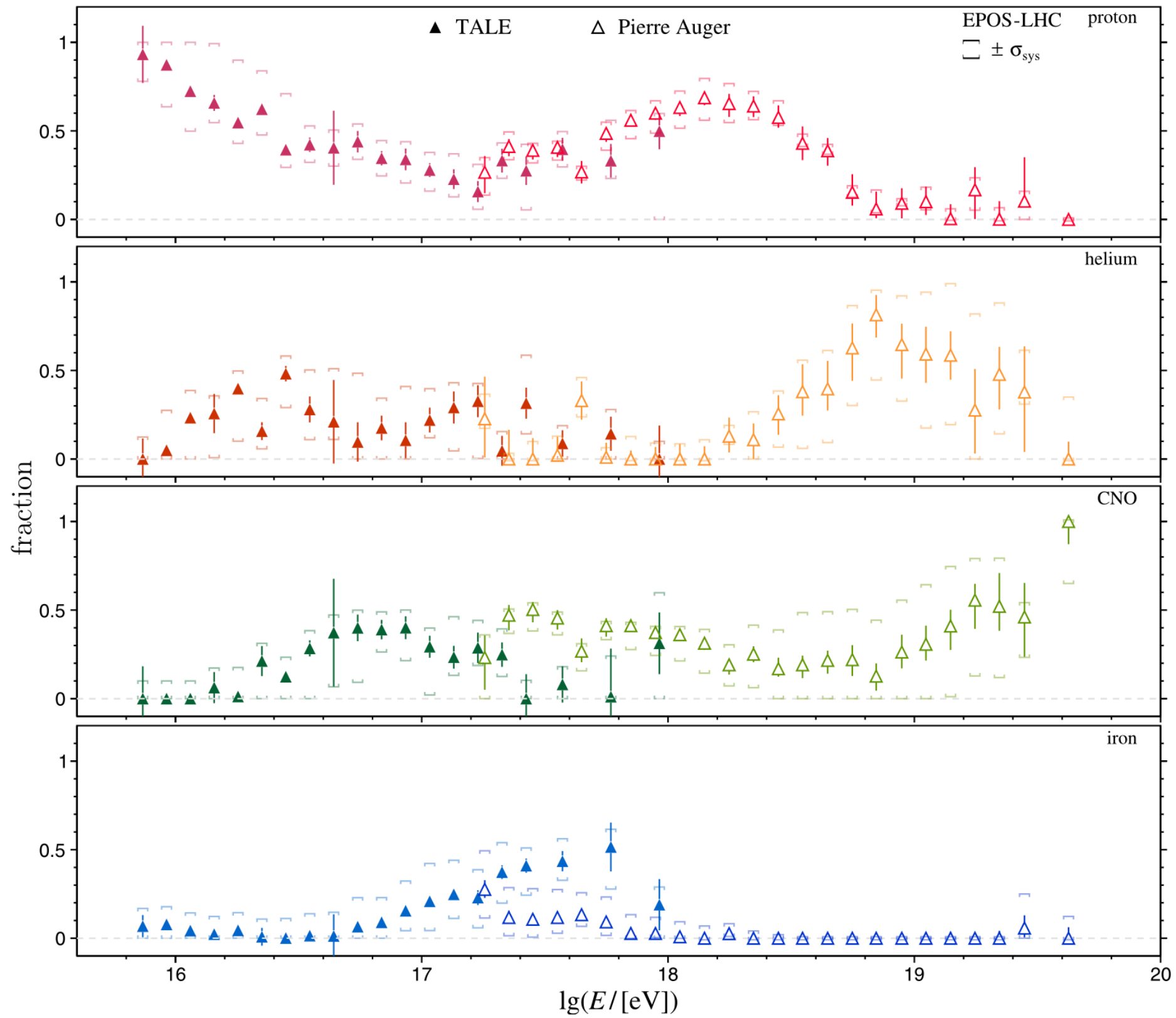


Fig. 14. Fractions of primary nuclei from the mass composition fits of X_{max} distributions measured at the Telescope Array (TALE) [143] and the Pierre Auger Observatory [187] inferred with EPOS-LHC.

Uncertainties of Standard Model Predictions for Muon Number and Production Depth

maximal variation of muon number N_μ and maximal muon production depth X_{\max}^μ taking into account collider data/constraints

S. Ostapchenko and G. Sigl, arXiv:2404.02085

“pion splitting”

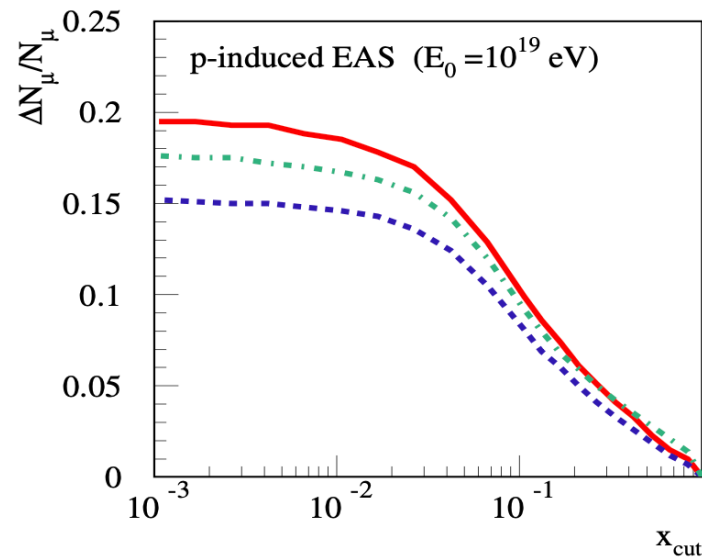


Figure 4: x_{cut} dependence of the relative change of N_μ ($E_\mu > 1$ GeV) at sea level EAS of $E_0 = 10^{19}$ eV, for the pion “splitting” procedure, for different interaction models II-04 (solid line), EPOS-LHC (dashed line), and SIBYLL-2.3 (dash-dotted line).

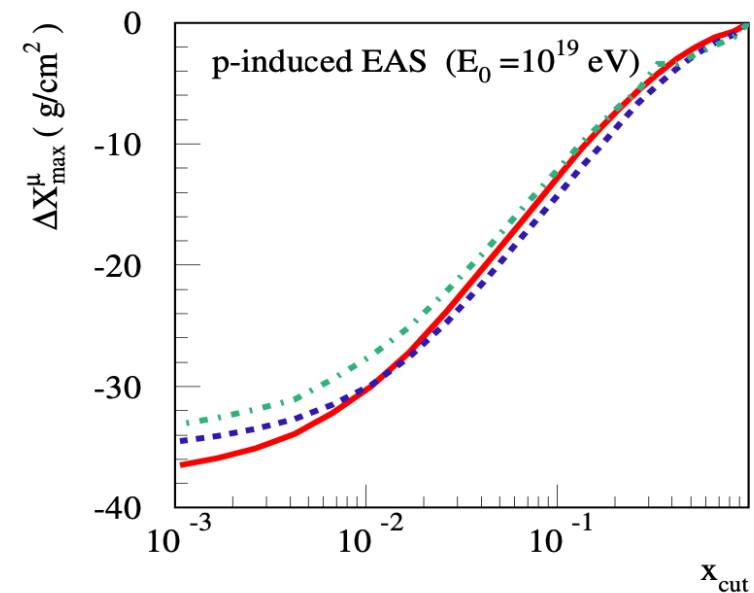


Figure 6: x_{cut} dependence for the modification of X_{\max}^μ by the pion “splitting” procedure, for p -induced EAS of $E_0 = 10^{19}$ eV, for different interaction models. The meaning of the lines is the same as in Fig. 4.

modified pion
exchange

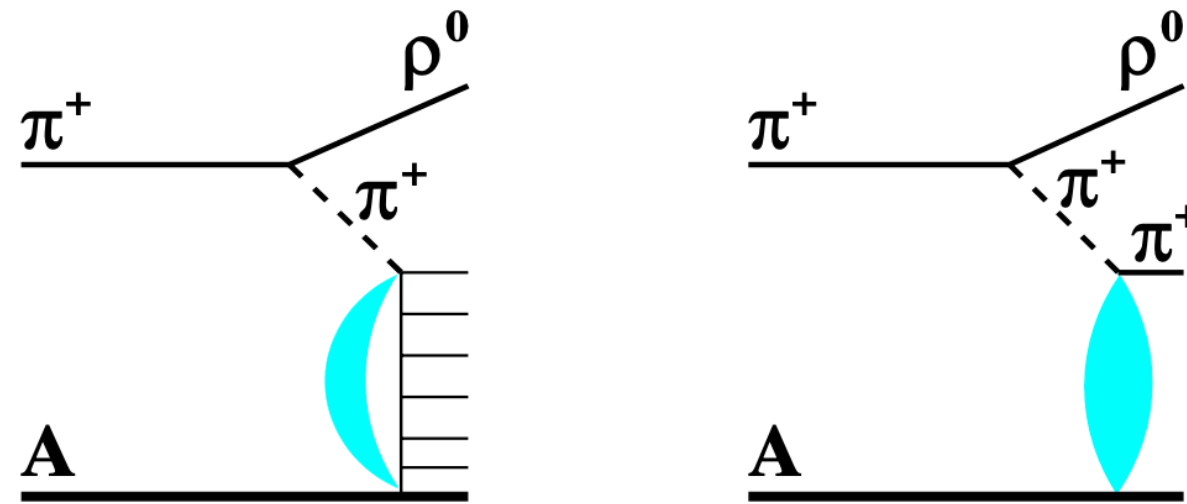


Figure 20: Schematic view of the two contributions to the pion exchange process: for inelastic scattering of the virtual pion (left), the leading ρ meson is accompanied by multiple hadron production; elastic scattering (right) gives rise to only one secondary pion, in addition to the ρ meson. The light shaded croissant and ellipsis correspond to contributions of elastic rescattering processes.

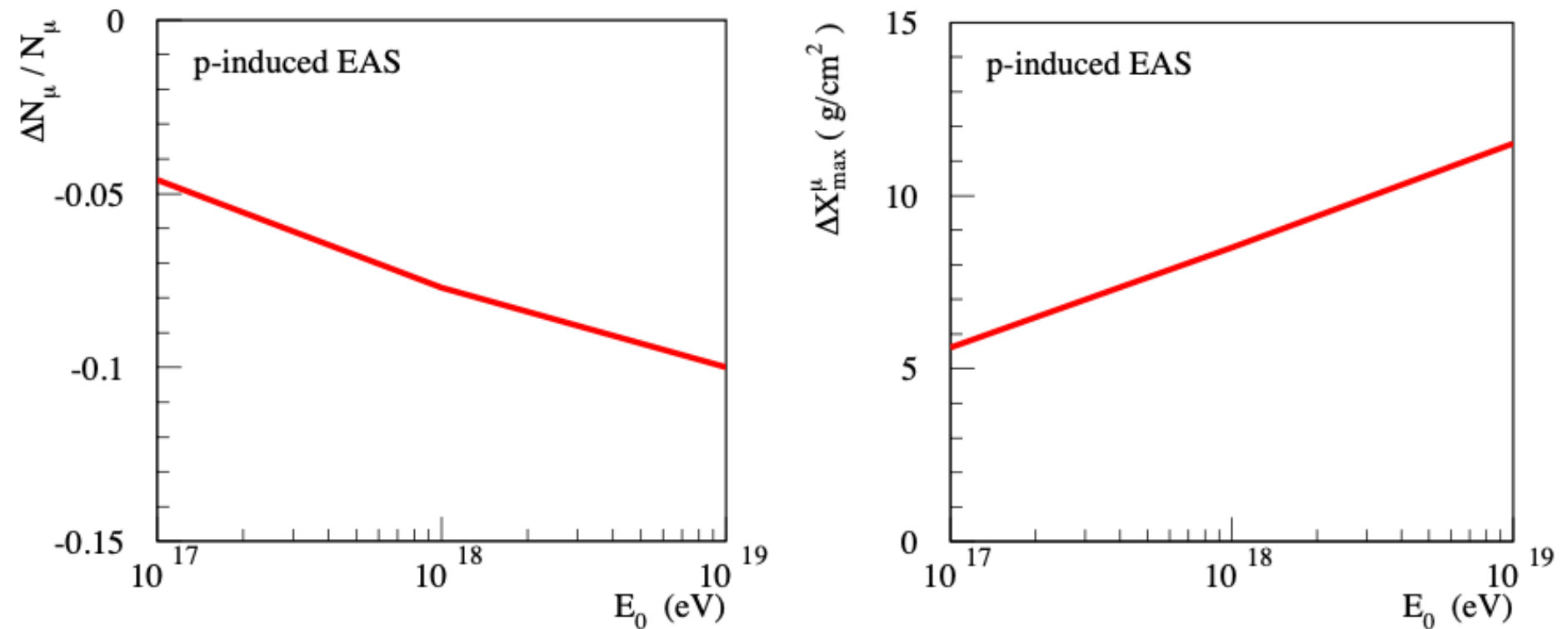


Figure 19: Energy dependence of the relative change of the muon number N_μ at sea level (left) and of the modification of the maximal muon production depth X_{\max}^μ (right), both for $E_\mu > 1$ GeV, for proton-initiated EAS, with respect to the corresponding predictions of the default QGSJET-III model, for the alternative treatment of the pion exchange process, discussed in the text.

enhanced (anti)nucleon, kaon and ρ meson production

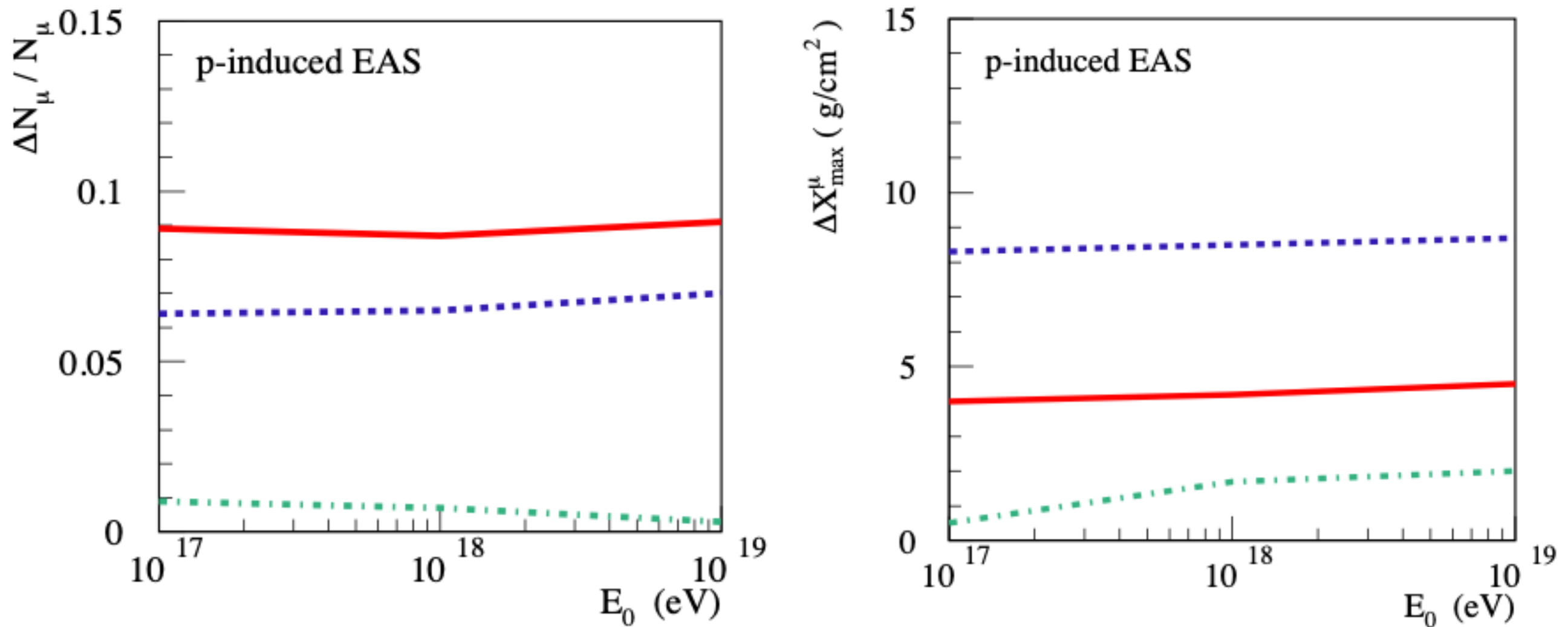


Figure 16: Energy dependence of the relative change of the muon number N_μ at sea level (left) and of the modification of the maximal muon production depth X_{\max}^μ (right), both for $E_\mu > 1$ GeV, for proton-initiated EAS, with respect to the corresponding predictions of the default QGSJET-III model, for the considered modifications of the model: enhancement of (anti)nucleon, kaon, and ρ meson production – solid, dashed, and dash-dotted lines, respectively.

Global Picture on Mass Composition

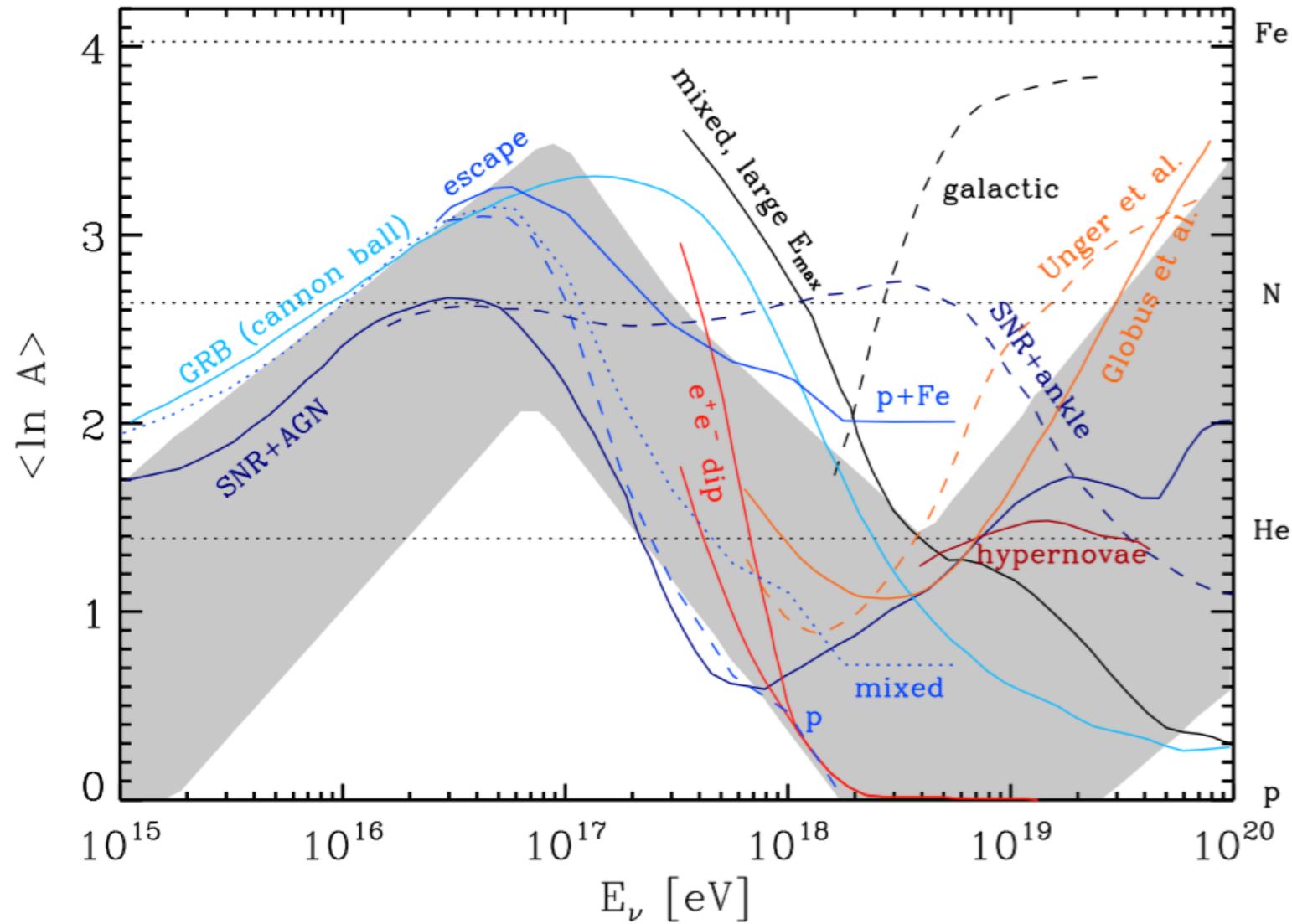


Fig. 5.8 The energy dependence of the average logarithmic mass predicted by various models, as indicated and explained in more details in the text. The grey band represents the combined uncertainties resulting from systematic experimental errors and hadronic model uncertainties, based on data such as the ones shown in Fig. 5.7. The first minimum in $\langle \ln A \rangle$ at $\simeq 3 \times 10^{15}$ eV corresponds to the CR knee and the first maximum in $\langle \ln A \rangle$ at $\simeq 10^{17}$ eV corresponds to the *second knee*. Both the knee and the second knee could signify a rigidity dependent Peters cycle either due to the maximal rigidity reached at acceleration in supernova remnants or due to a transition to a propagation regime leading to faster CR leakage from the Galaxy. Finally, the second minimum in $\langle \ln A \rangle$ at $\simeq 5 \times 10^{18}$ eV signifies the *ankle*. Compare the CR spectrum shown in Fig. 5.6. Inspired by Ref. [231].

Indications of "Peters cycles" for galactic and extragalactic sources whose maximal energies are proportional to the charge Z and extend up to $\sim 10^{17}$ and 10^{20} eV, respectively

G. Sigl, book "Astroparticle Physics: Theory and Phenomenology", Atlantis Press/Springer 2016

see also K.-H.Kampert and M.Unger, *Astropart.Phys.* 35 (2012) 660

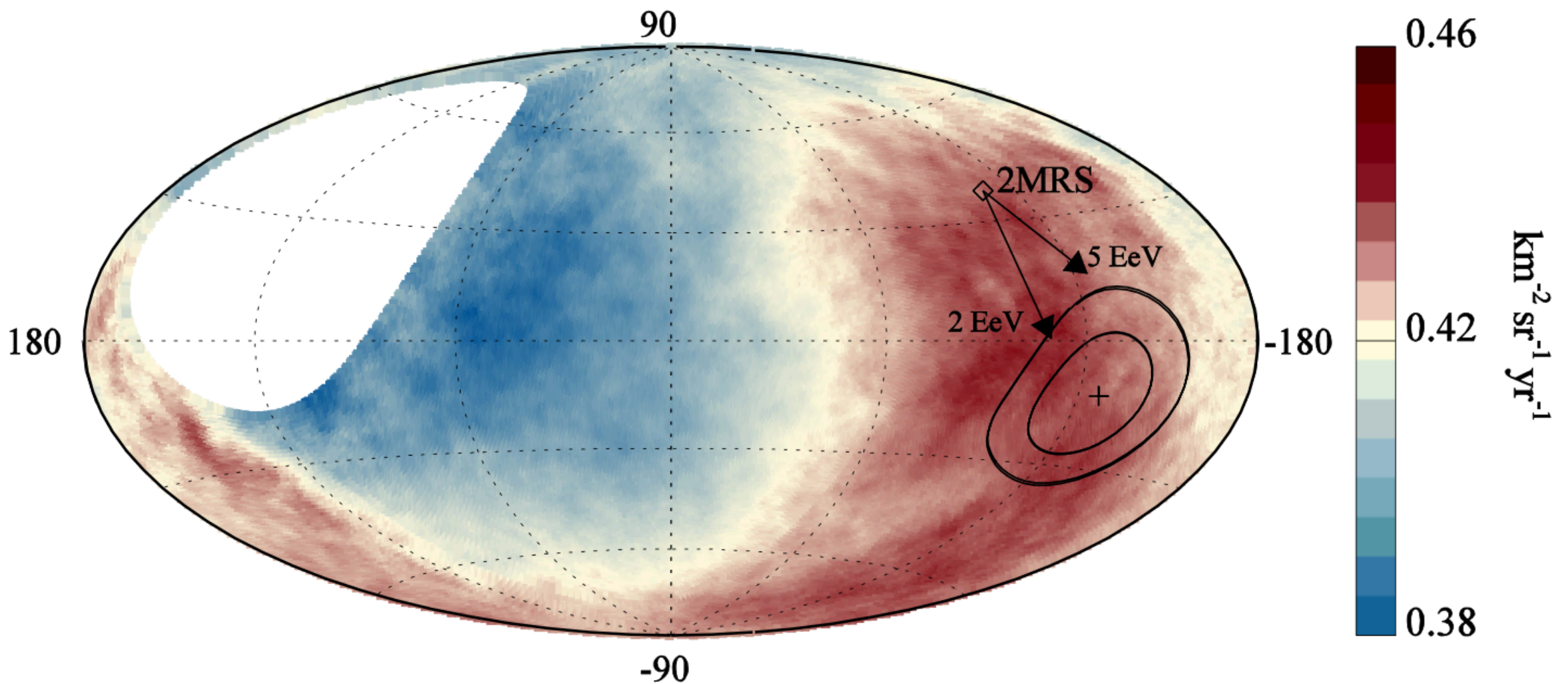
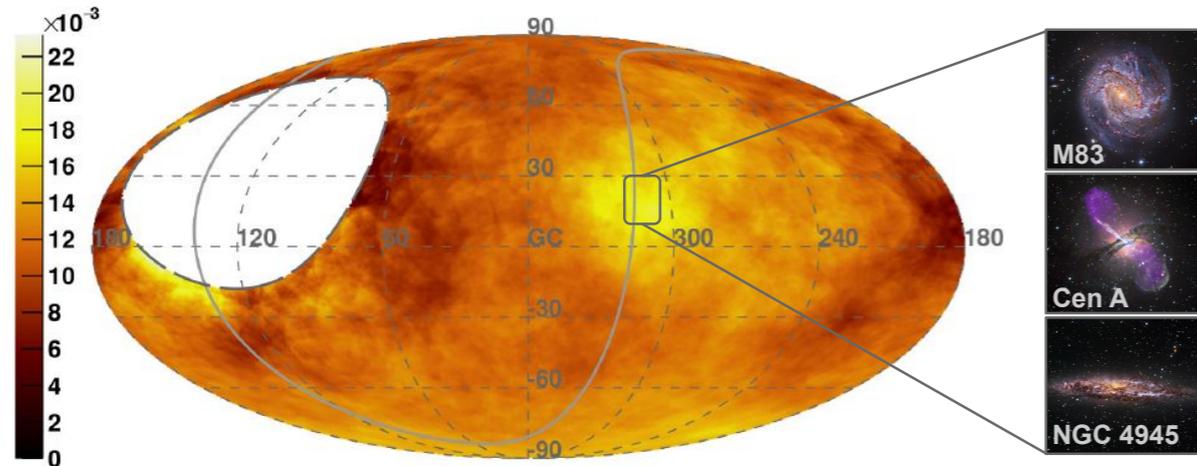


Fig. 3. Map showing the fluxes of particles in Galactic coordinates. Sky map in Galactic coordinates showing the cosmic-ray flux for $E \geq 8$ EeV smoothed with a 45° top-hat function. The Galactic center is at the origin. The cross indicates the measured dipole direction and the contours the 68% and 95% confidence-level regions. The dipole in the 2MRS galaxy distribution is indicated, while arrows show the deflections expected for a particular model of the Galactic magnetic field (8), for $E/Z=5$ EeV or 2 EeV.

Anisotropy searches at highest energies – catalogs

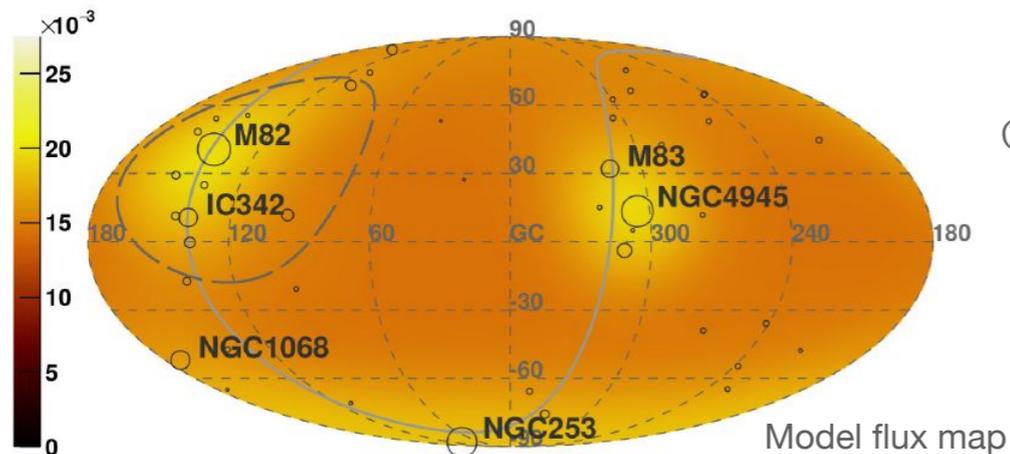
$\Phi(E_{\text{Auger}} > 41 \text{ EeV}) [\text{km}^{-2} \text{sr}^{-1} \text{yr}^{-1}]$ - Galactic coordinates - $\Psi = 24^\circ$



Direction fixed to that of Cen A, free E_{th} and Ψ

$E_{\text{th}} > 41 \text{ EeV}$, $\Psi = 27^\circ$: **3.9 σ post-trial** deviation from isotropy (5% excess)

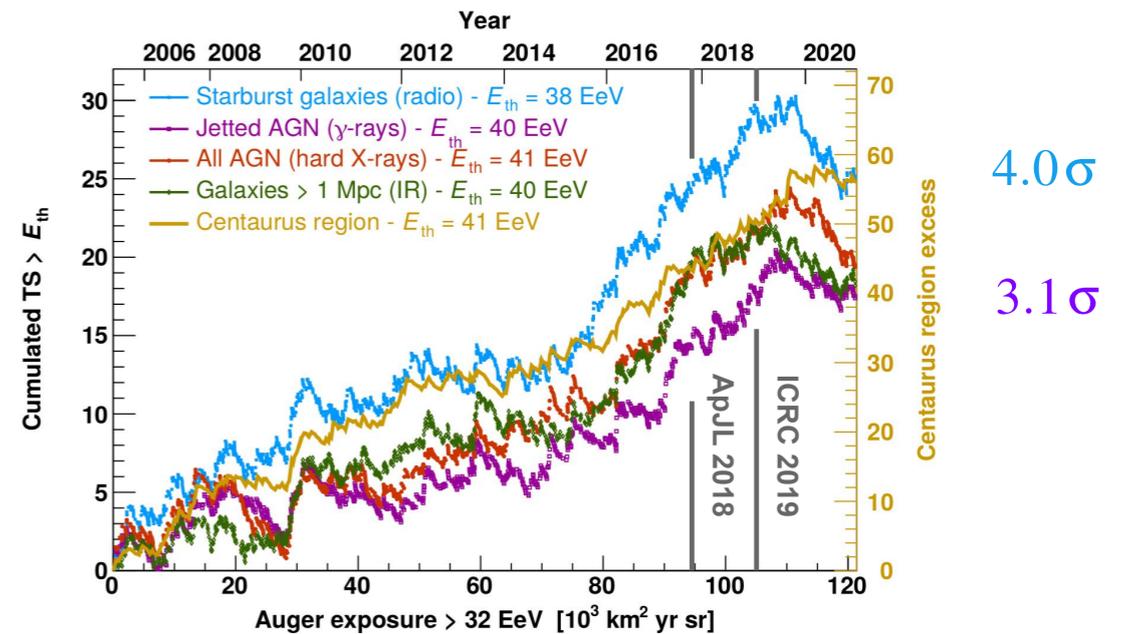
Starburst galaxies (radio) - expected $\Phi(E_{\text{Auger}} > 38 \text{ EeV}) [\text{km}^{-2} \text{sr}^{-1} \text{yr}^{-1}]$



(Jonathan Biteau)

All data until end of 2020, optimized quality cuts: 120,000 km² sr yr

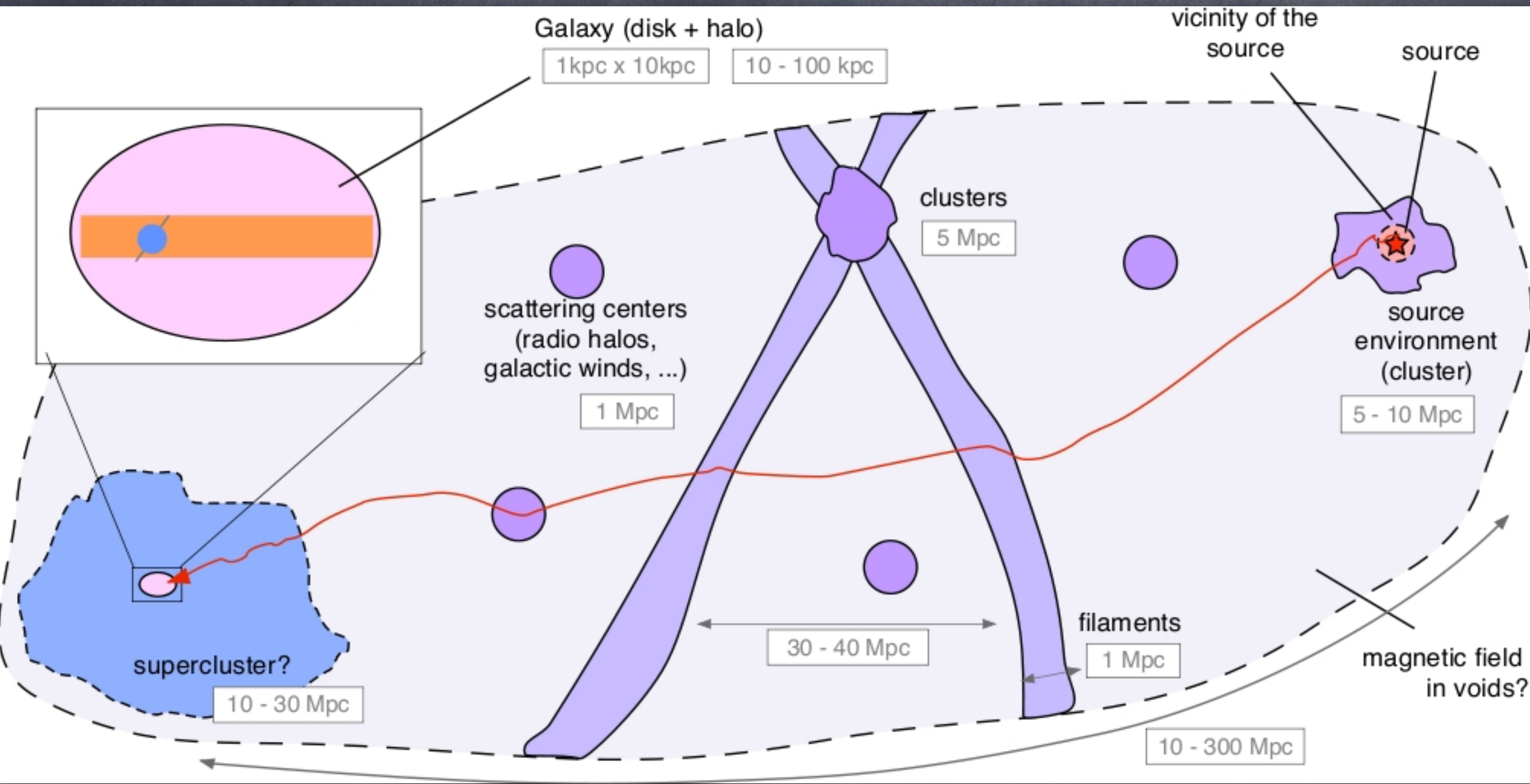
Catalog	E_{th} [EeV]	Ψ [deg]	α [%]	TS	Post-trial p -value
All galaxies (IR)	40	24^{+16}_{-8}	15^{+10}_{-6}	18.2	6.7×10^{-4}
Starbursts (radio)	38	25^{+11}_{-7}	9^{+6}_{-4}	24.8	3.1×10^{-5}
All AGNs (X-rays)	41	27^{+14}_{-9}	8^{+5}_{-4}	19.3	4.0×10^{-4}
Jetted AGNs (γ -rays)	40	23^{+9}_{-8}	6^{+4}_{-3}	17.3	1.0×10^{-3}



Growth of test statistic (TS) compatible with linear increase
Discovery threshold of 5 σ expected in 2025 – 2030 (Phase II)
Other means to increase sensitivity (Auger 85% sky coverage)

taken from R. Engel, Pierre Auger highlights, ICRC 2021, see also Pierre Auger collaboration, *Astrophys. J.* 935 (2022) 170

3-Dimensional Effects in Propagation



Kotera, Olinto, *Ann.Rev.Astron.Astrophys.* 49 (2011) 119

Extragalactic Magnetic Field Filling Factors from recent Simulations

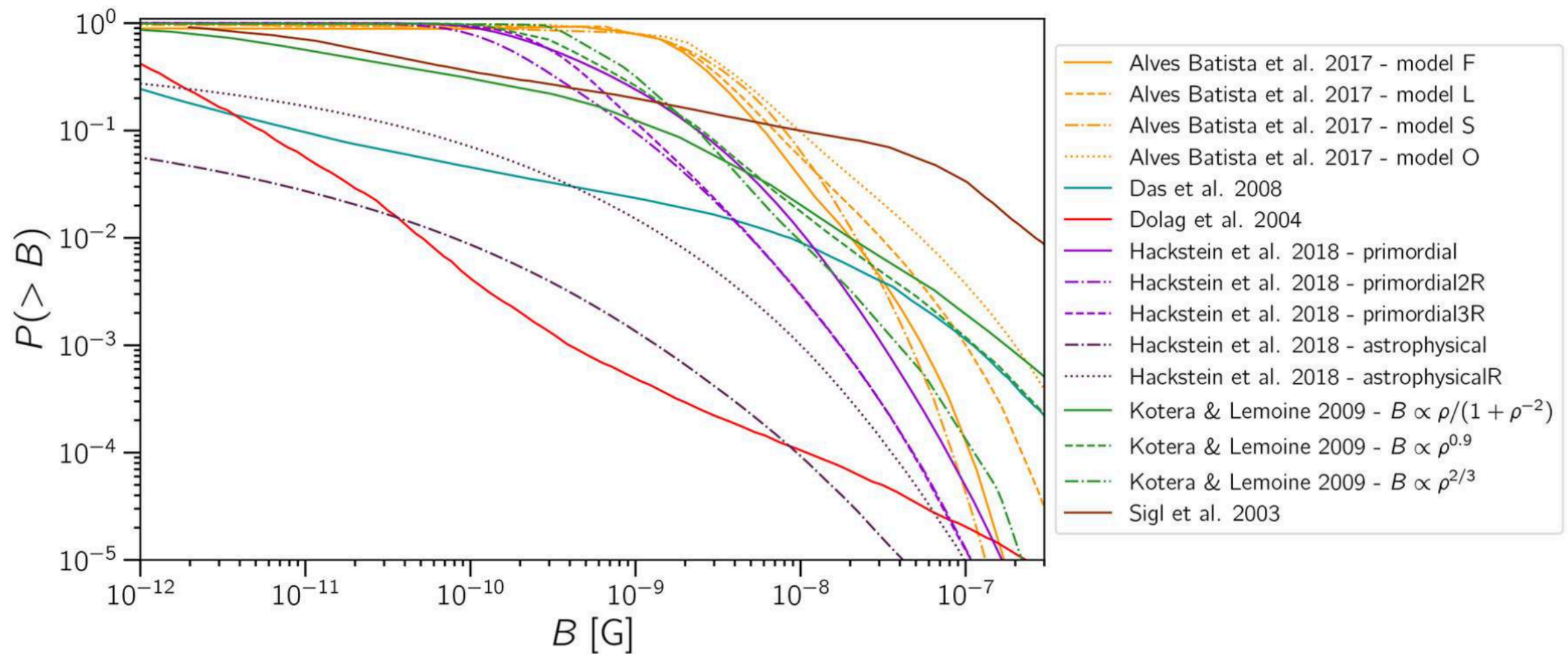
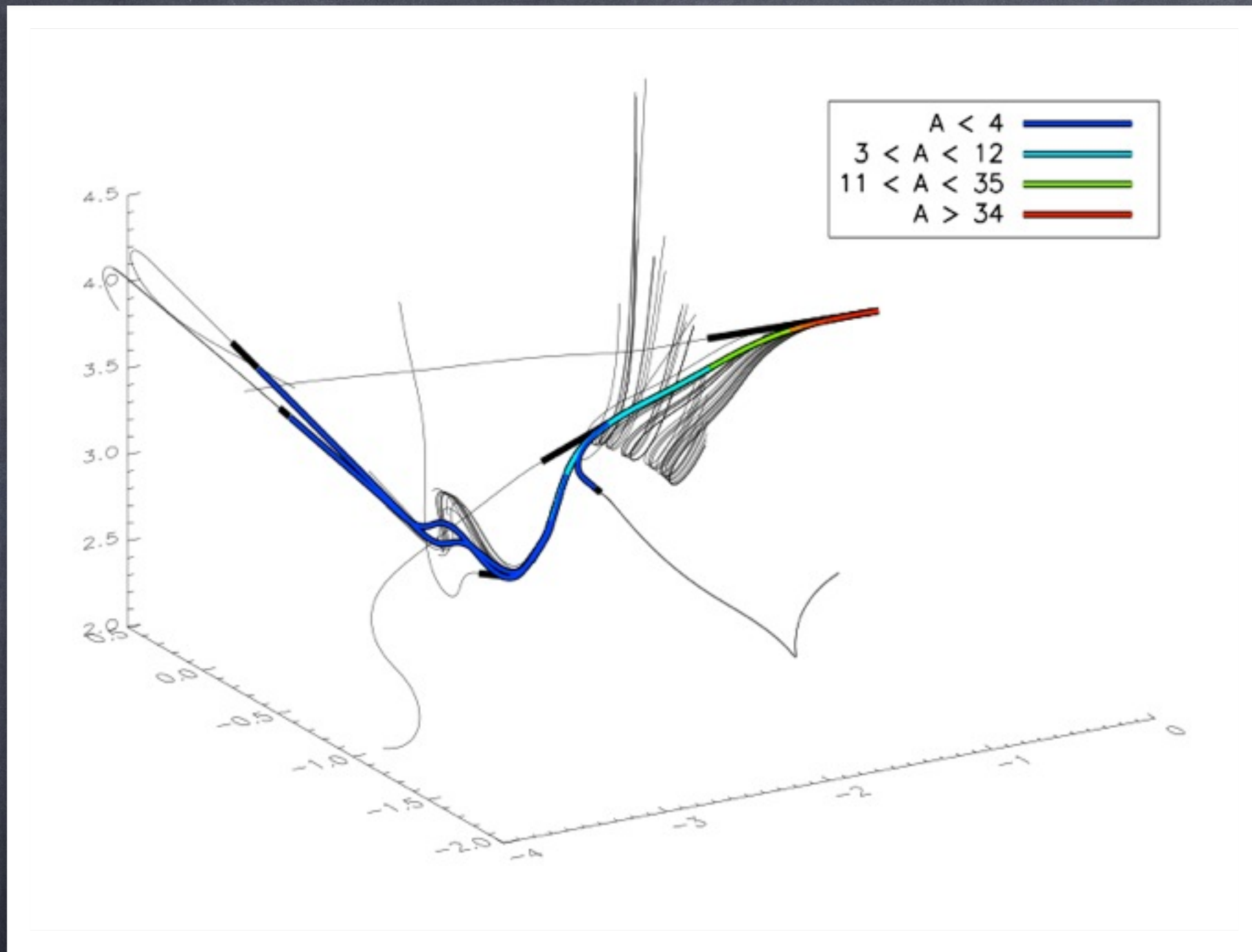


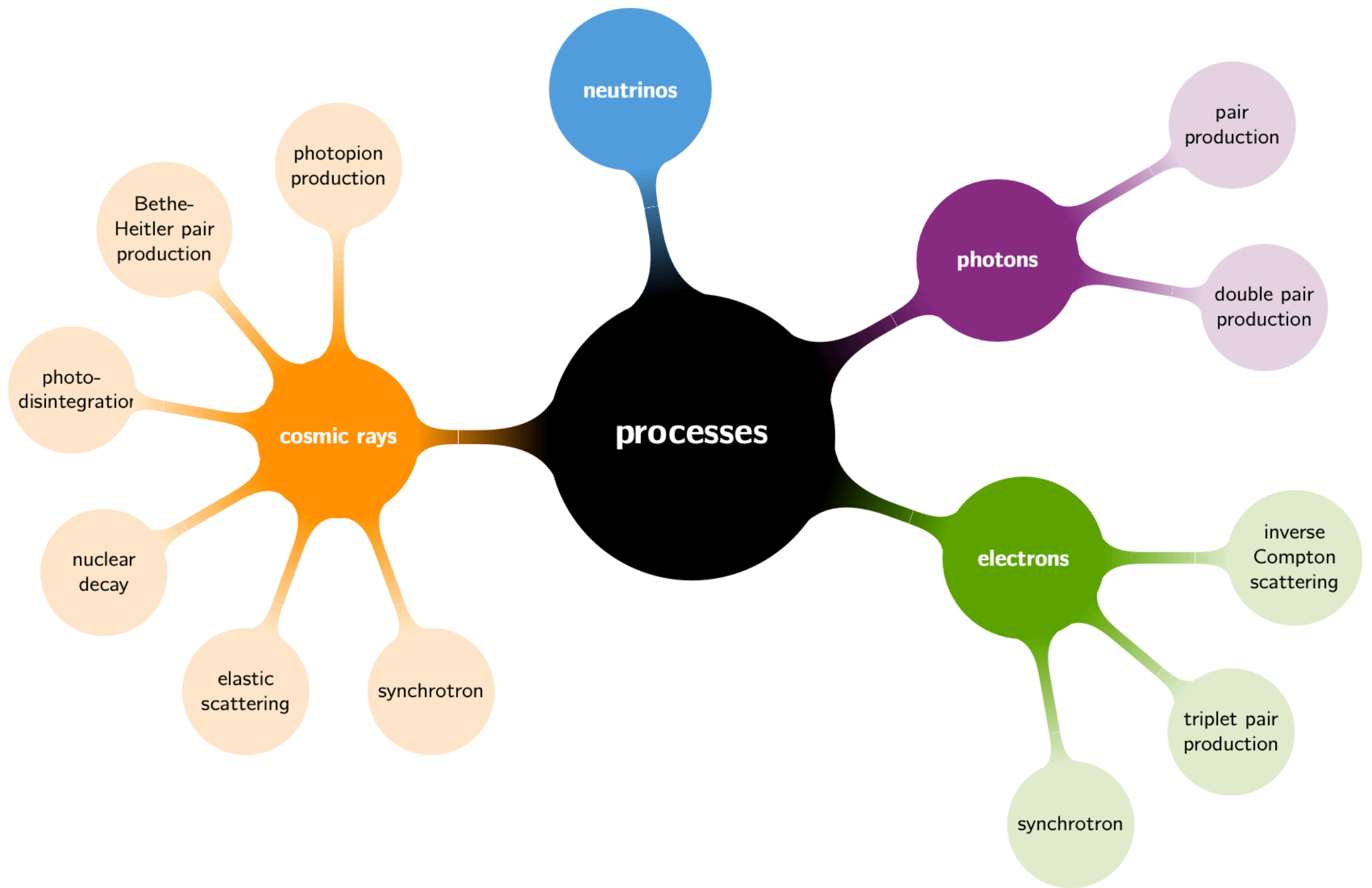
FIGURE 15 | Cumulative volume filling factors for EGMFs according to several models. Details about each model can be found in the corresponding publications: Alves Batista et al. (2017), Das et al. (2008), Dolag et al. (2005), Hackstein et al. (2018), Kotera and Lemoine (2008a), and Sigl et al. (2003b). R. Alves Batista for this review.

Alves Batista et al., "Open Questions in Cosmic Ray Research at ultra-high energies", *Front.Astron.Space Sci.* 6 (2019) 23 [arXiv:1903.06714]

Extragalactic iron propagation produces nuclear cascades in structured magnetic fields:



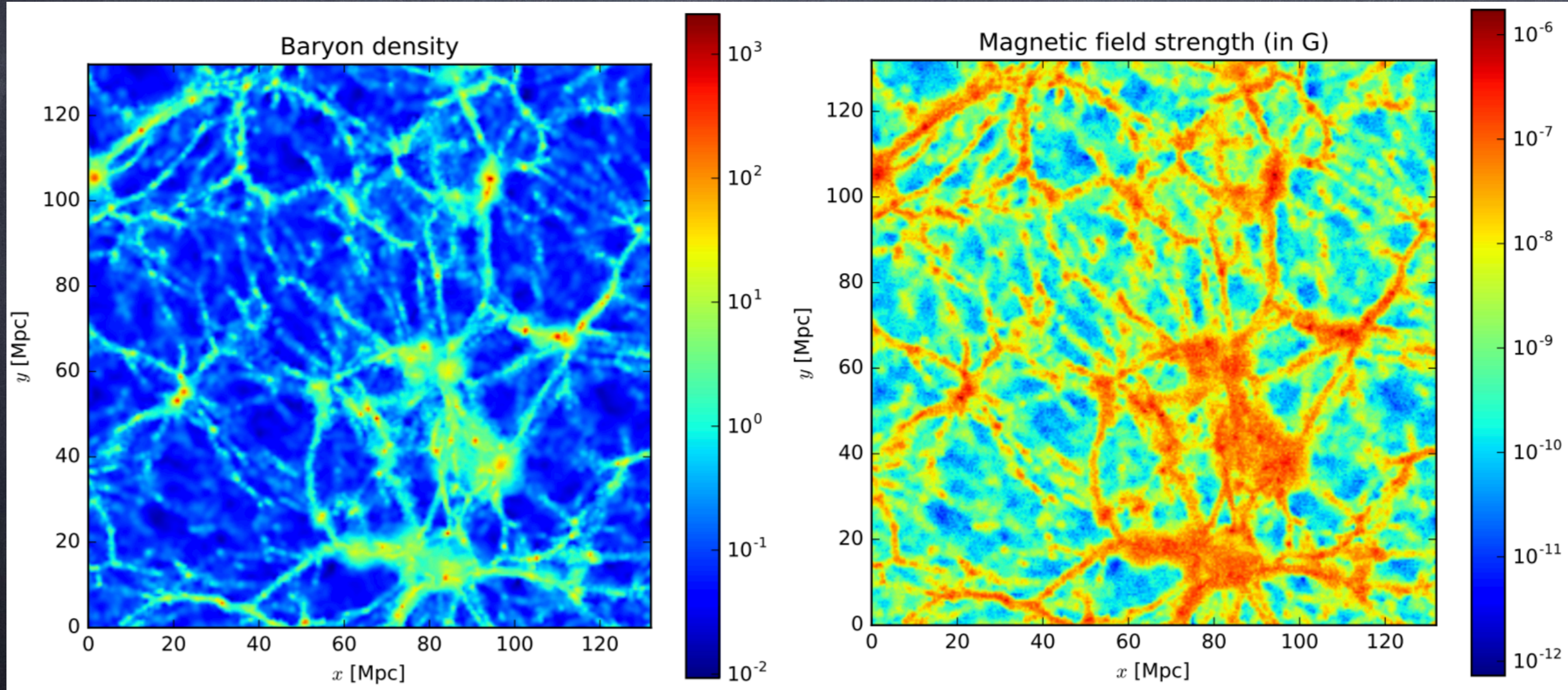
Initial energy 1.2×10^{21} eV, magnetic field range 10^{-15} to 10^{-6} G. Color-coded is the mass number of secondary nuclei



[https://crpropa.desy.de/Main Page](https://crpropa.desy.de/Main_Page)

<https://github.com/CRPropa/CRPropa3/>

Discrete Sources in nearby large scale structure



Some General Considerations

Propagation Theorem/Liouville Theorem

A homogeneous distribution of sources with equal properties and nearest neighbour distances smaller than other relevant length scales in the problem such as energy loss length and propagation/diffusion length within the source activity time scale gives rise to a universal/isotropic flux spectrum that does not depend on the propagation mode and thus on the magnetic field properties.

Easiest to see in the back-tracking picture:

The differential flux in the direction characterised by the unit vector \mathbf{n} at observer position \mathbf{r}_0 is given by

$$j(E_0, \mathbf{r}_0, \mathbf{n}) = \int_{t_0}^{t_{\max}} dt \dot{\rho} [E(t), t, \mathbf{r}(t, \mathbf{n})] ,$$

where $\dot{\rho}(E, t, \mathbf{r})$ is the differential injection rate at energy E , time t , and location \mathbf{r} , $\mathbf{r}(t, \mathbf{n})$ is the back-tracked trajectory with the initial conditions $\mathbf{r}(t_0, \mathbf{n}) = \mathbf{r}_0$, $\dot{\mathbf{r}}(t_0, \mathbf{n}) = \mathbf{n}$ and $E(t)$ with $E(t_0) = E_0$ is the back-tracked energy. For stochastic losses one has to average over trajectories with equal initial conditions.

Clearly, if $\dot{\rho}$ only depends on E and t , then the flux neither depends on the shape of the trajectories nor on direction, but only on energy, and thus is universal.

This also applies to secondary fluxes such as neutrinos and gamma-rays because densities only depend on the time-integrated interaction rates (and energy loss rates) which are location independent

Corollary:

To be sensitive to the propagation mode, magnetic field structure etc. requires discrete, inhomogeneous source distributions with nearest-neighbour distances larger than energy loss length and/or propagation distance within source activity time

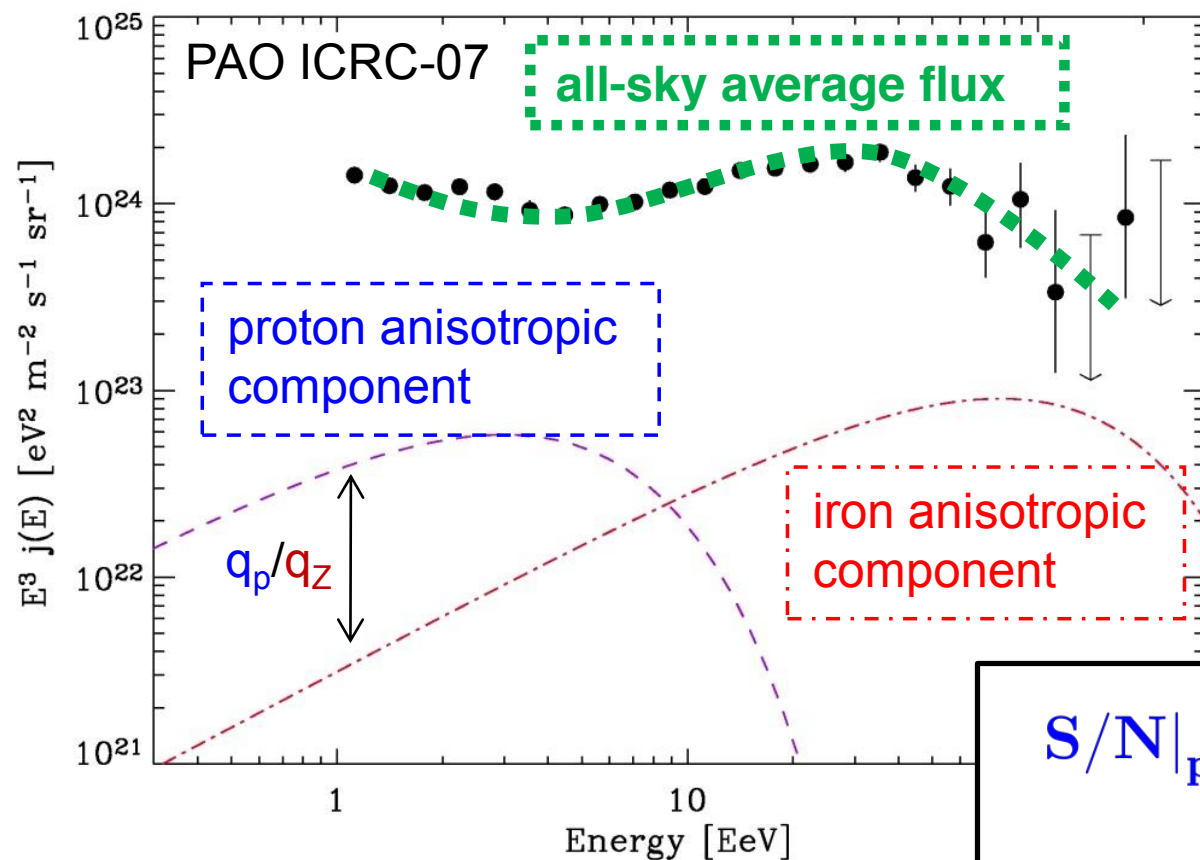
Modelling Challenges

- Broad dynamic range in length and time scales
- partly unknown propagation mode: ballistic versus diffusive
- disentangling source distribution/rates from propagation mode

Anisotropies vs heavy composition at UHE



→ if anisotropic signal $>E$ is due to heavy nuclei, one should detect a **stronger anisotropy signal associated with protons of same magnetic rigidity at $>E/Z$ eV...**
argument independent of intervening magnetic fields... (M.L. & Waxman 09, Liu+13)



Compare strength of anisotropy at E and E/Z:

$$S/N|_p (> E/Z) \simeq \underbrace{\alpha_{\text{loss},Z}}_{>1} \underbrace{Z^{-0.85}}_{<1} \underbrace{\frac{N_p}{N_Z}}_{\gg 1} S/N|_Z (> E)$$

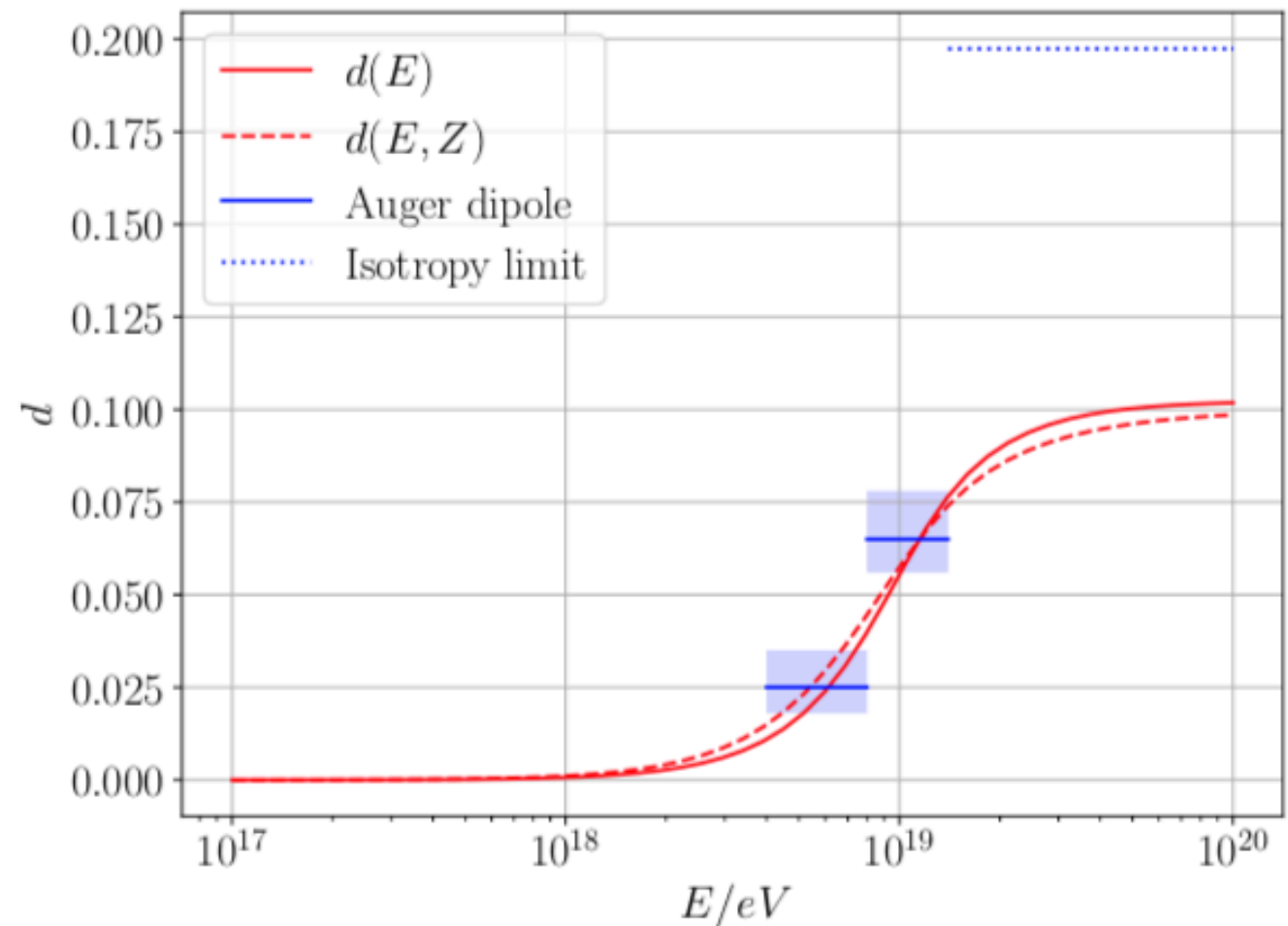
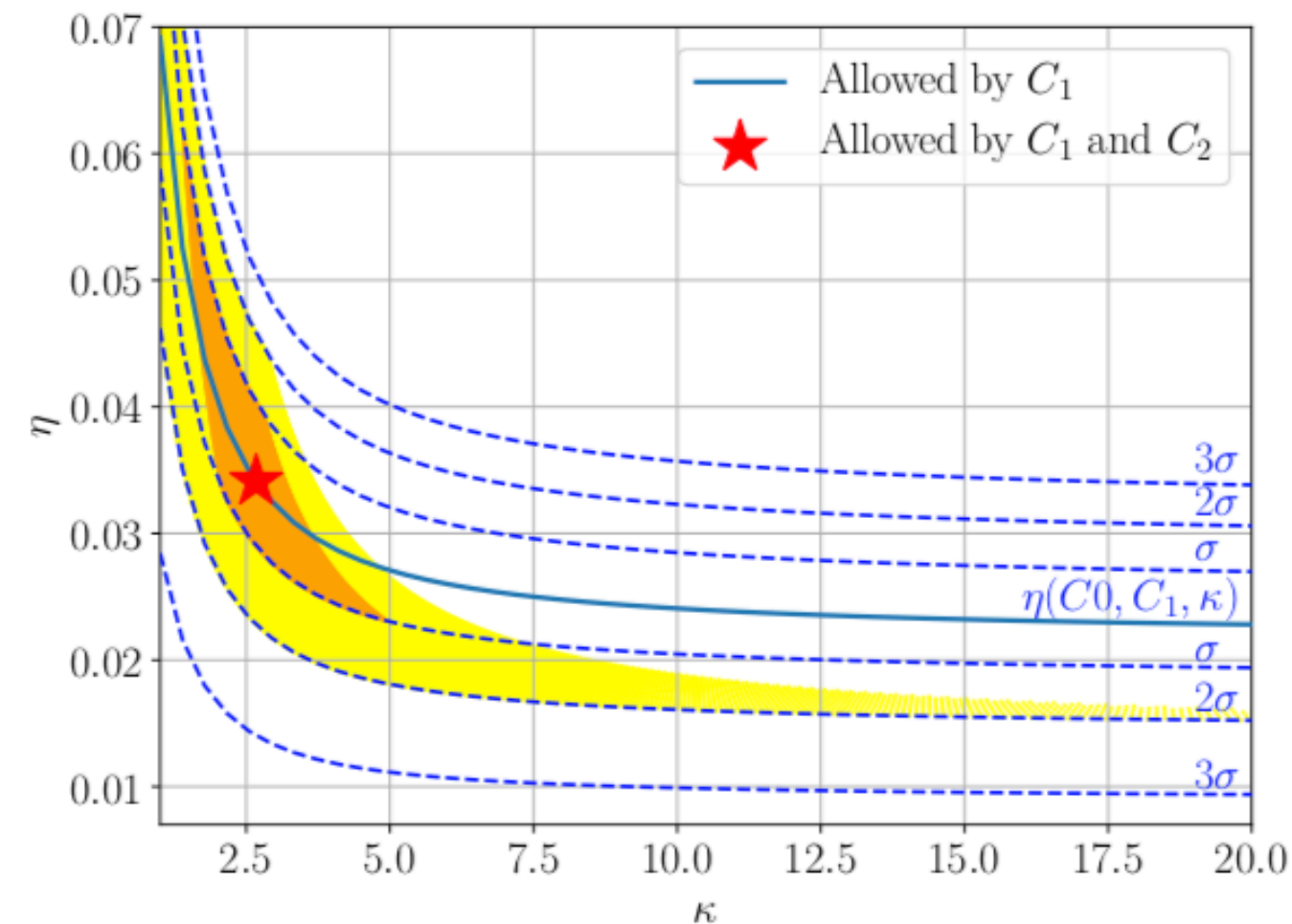
$\gg 1$

→ if anisotropies are seen at $E \sim \text{GZK}$, but not at E/Z :

- **there exist protons at GZK producing the anisotropies...**
- **or, if Fe at UHE: $Z \gtrsim 1000 Z_0$... if Si at UHE: $Z \gtrsim 1600 Z_0$... if O at UHE: $Z \gtrsim 100 Z_0$**
 ... sources with such high metallicities?

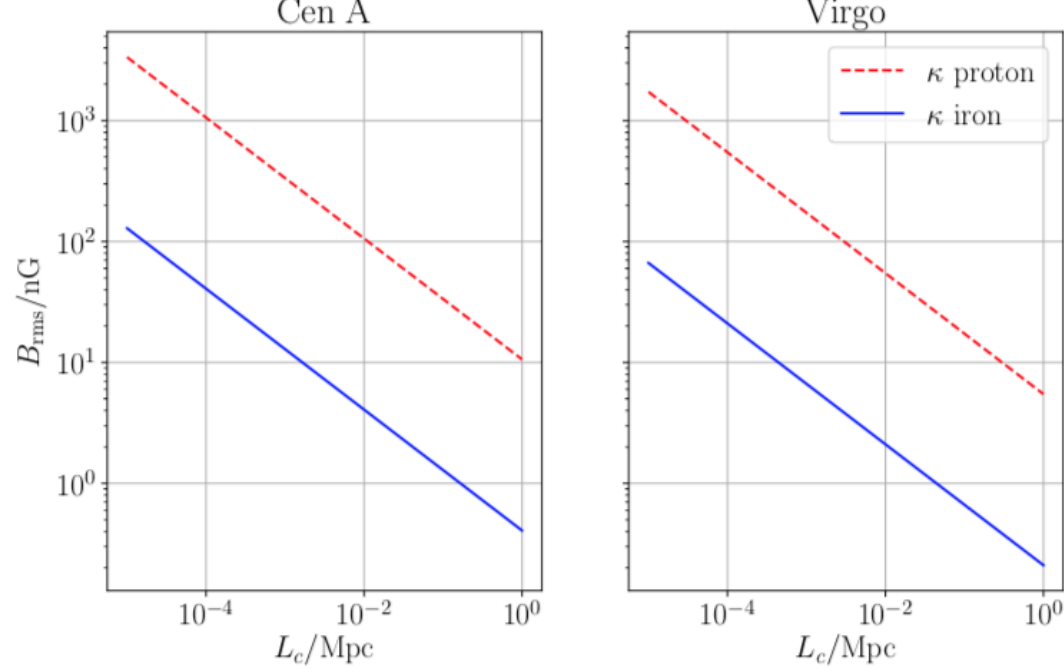
A Simple One Source + Isotropic Background Model

Contribution of the one discrete source to the total flux parametrised by η and deflection spread by concentration parameter κ : Dipole and quadrupole can fix both parameters, e.g. C_2/C_1 fixes κ



best fit $\eta \sim 0.035$, $\kappa \sim 2.5$, corresponding to a spread of ~ 50 degrees.

Dundovic and Sigl, JCAP 1901 (2019) 018 [arXiv:1710.05517]



Dundovic and Sigl, JCAP 1901 (2019) 018
[arXiv:1710.05517]

Figure 12. For a source of a given distance, the remaining parameters left undetermined are charge, magnetic field strength and coherence length. The plot shows the relation between B_{rms} and L_c following from eq. 3.4 for the fitted value of κ , for proton and iron primaries coming from Centaurus A and the Virgo cluster.

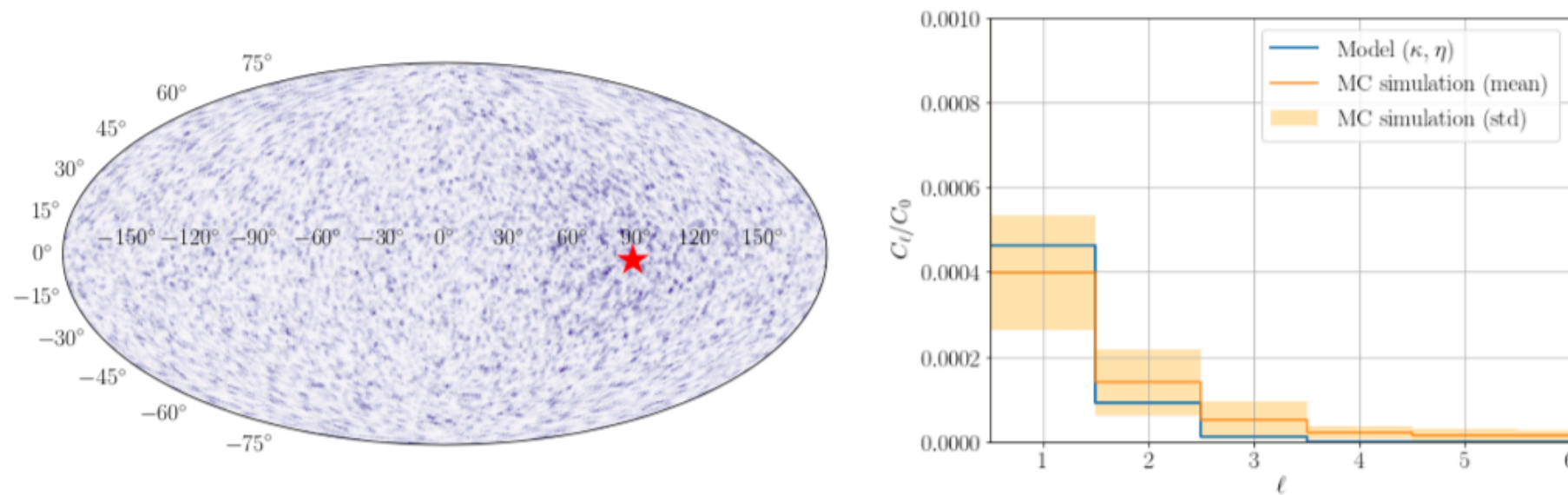


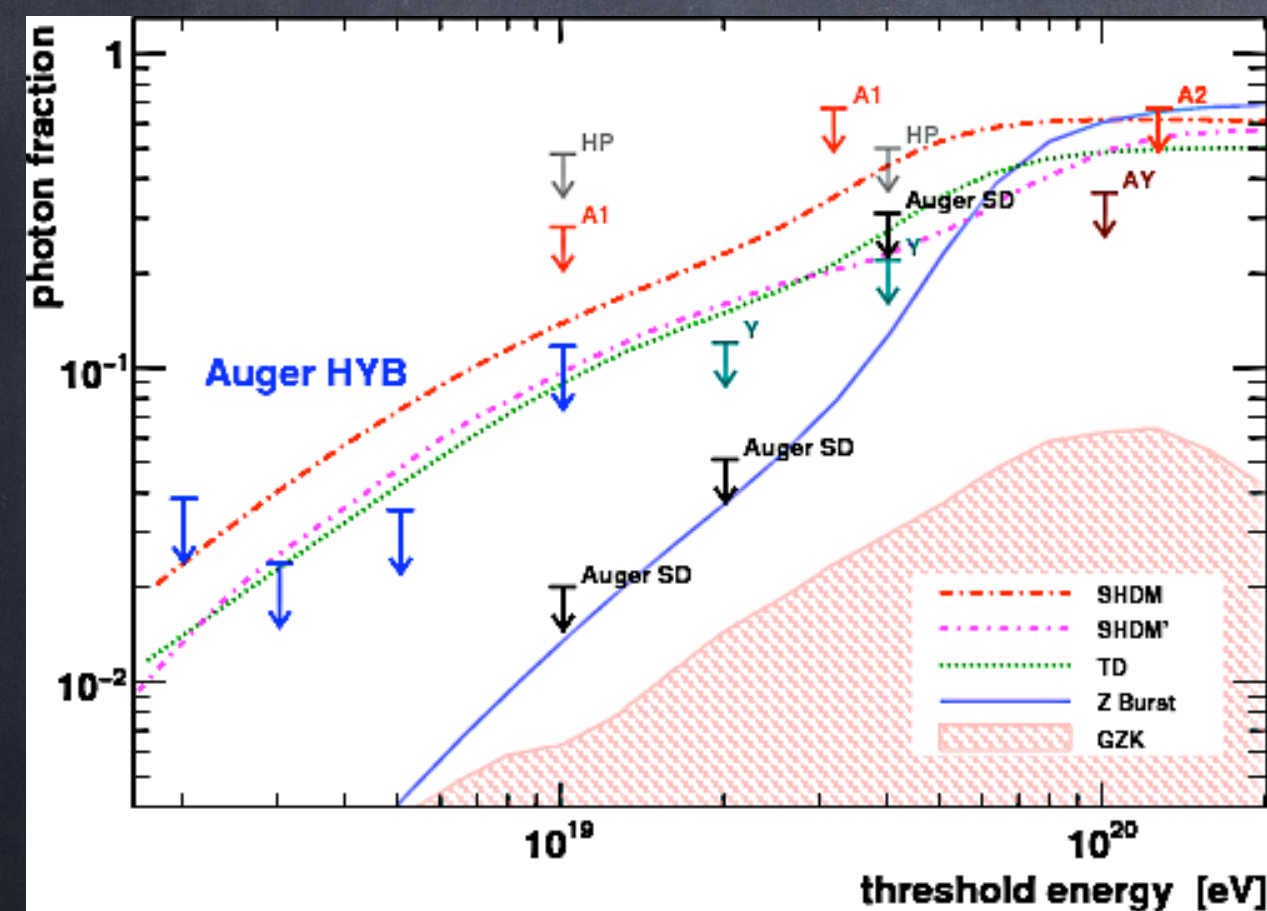
Figure 13. The two plots are results of a Monte Carlo simulation which is set up as described in the text. The sky plot shows the dipole induced by the single source which is placed at 4 Mpc distance from the observer. The direction of the dipole is marked with the star. Other parameters are $Z = 26$, $E = 11.5 E_{\text{TeV}}$, $B_{\text{rms}} = 2.9 \text{ nG}$, $L_c = 30 \text{ kpc}$, $\eta = 0.03$ where $(1 - \eta)$ is the isotropic contribution from the background. The right panel plot depicts the first few moments of the angular power spectrum where the blue line is the analytically calculated spectrum by using the spread parameter (κ) and the relative flux (η), while the orange line is a fit from the simulation. The orange shaded area represents one sigma fluctuations.

Lorentz Symmetry Violation in the Electromagnetic Sector

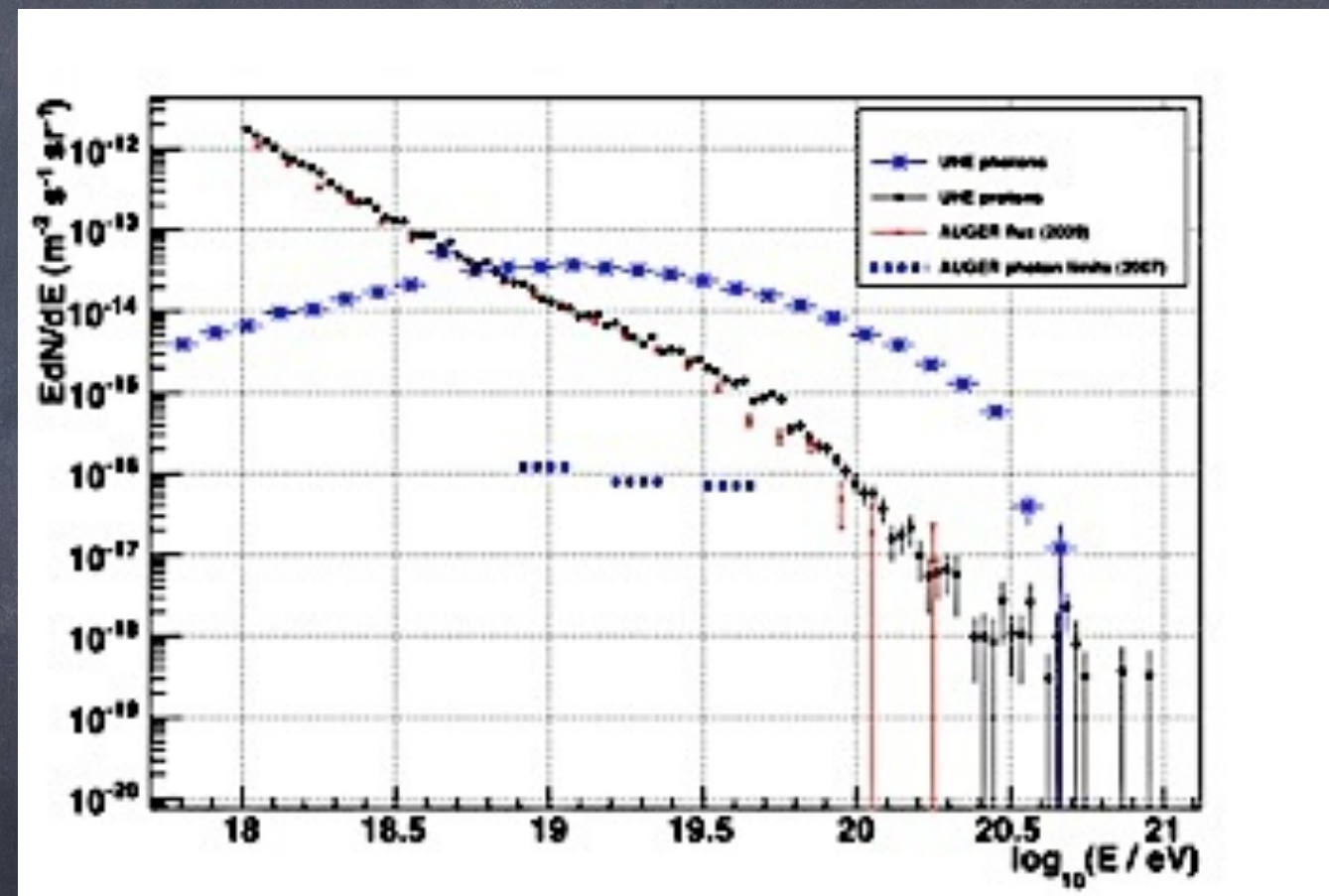
The idea:

Experimental upper limits on UHE photon fraction

Contradict predictions if pair production is absent



Pierre Auger Collaboration,
Astropart. Phys. 31 (2009) 399



Maccione, Liberati, Sigl,
PRL 105 (2010) 021101

Lorentz Symmetry Violation in the Photon Sector

For a photon dispersion relation

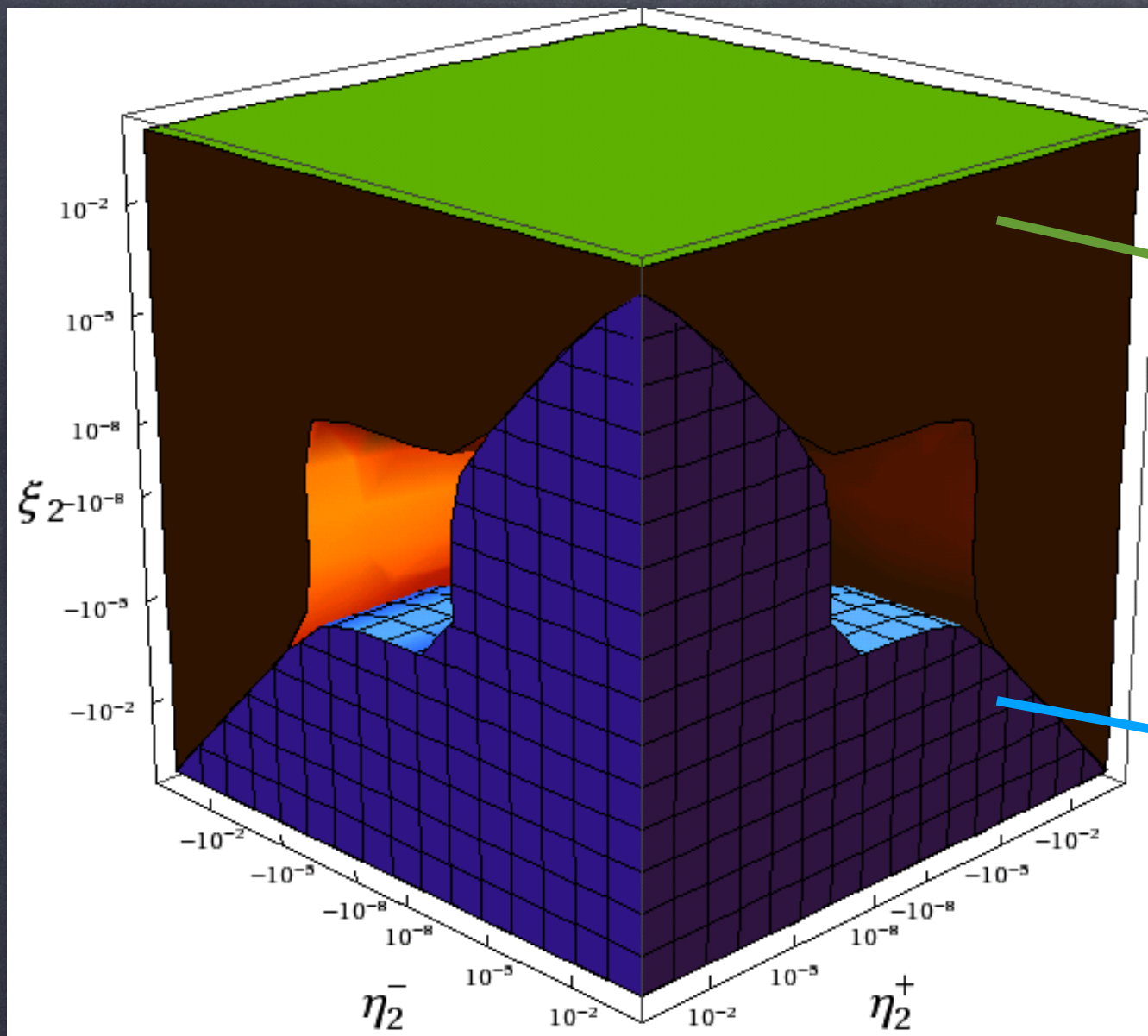
$$\omega_{\pm}^2 = k^2 + \xi_n^{\pm} k^2 \left(\frac{k}{M_{\text{Pl}}} \right)^n, n \geq 1,$$

pair production may become inhibited, increasing GZK photon fluxes above observed upper limits: In the absence of LIV for electrons/positrons for $n=1$ (CPT-odd terms) this yields:

$$\xi_1 \leq 10^{-12}$$

Even for $n=2$ (CPT-even) one has sensitivity to $\xi_2 \sim 10^{-6}$

Such strong limits may indicate that Lorentz invariance violations are completely absent !



Constraints for $n=2$ for the 3 independent parameters

excluded if UHE photons are detected

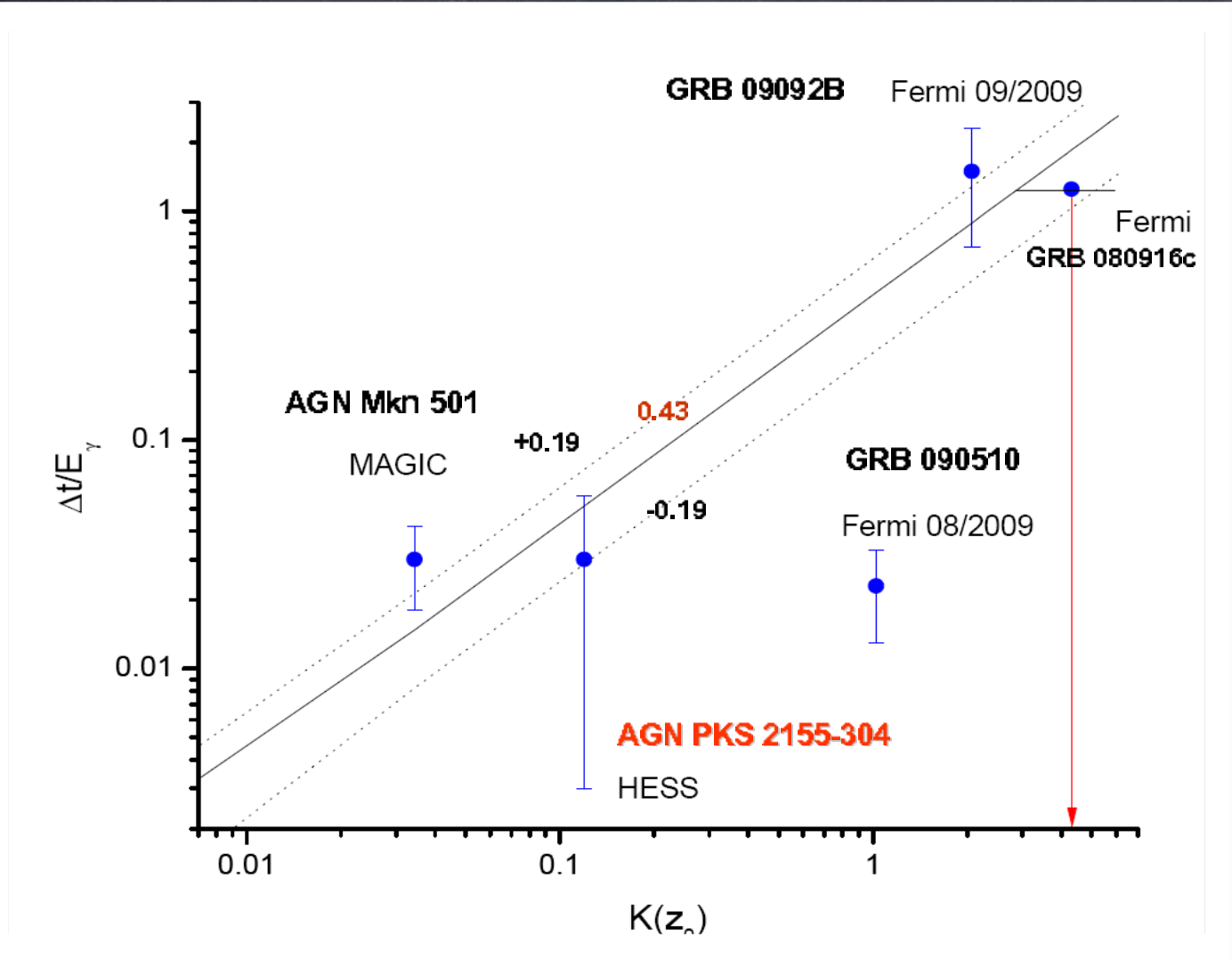
excluded by current photon flux upper limits/too little UHE photon absorption takes place

Such strong limits suggest that Lorentz invariance violations are completely absent !

The modified dispersion relation also leads to energy dependent group velocity $V = \partial E / \partial p$ and thus to an energy-dependent time delay over a distance d :

$$\Delta t = -\xi d \frac{E}{M_{\text{Pl}}} \simeq -\xi \left(\frac{d}{100 \text{ Mpc}} \right) \left(\frac{E}{\text{TeV}} \right) \text{ sec}$$

for linearly suppressed terms. GRB observations in TeV γ -rays can therefore probe quantum gravity and may explain that higher energy photons tend to arrive later (Ellis et al.).

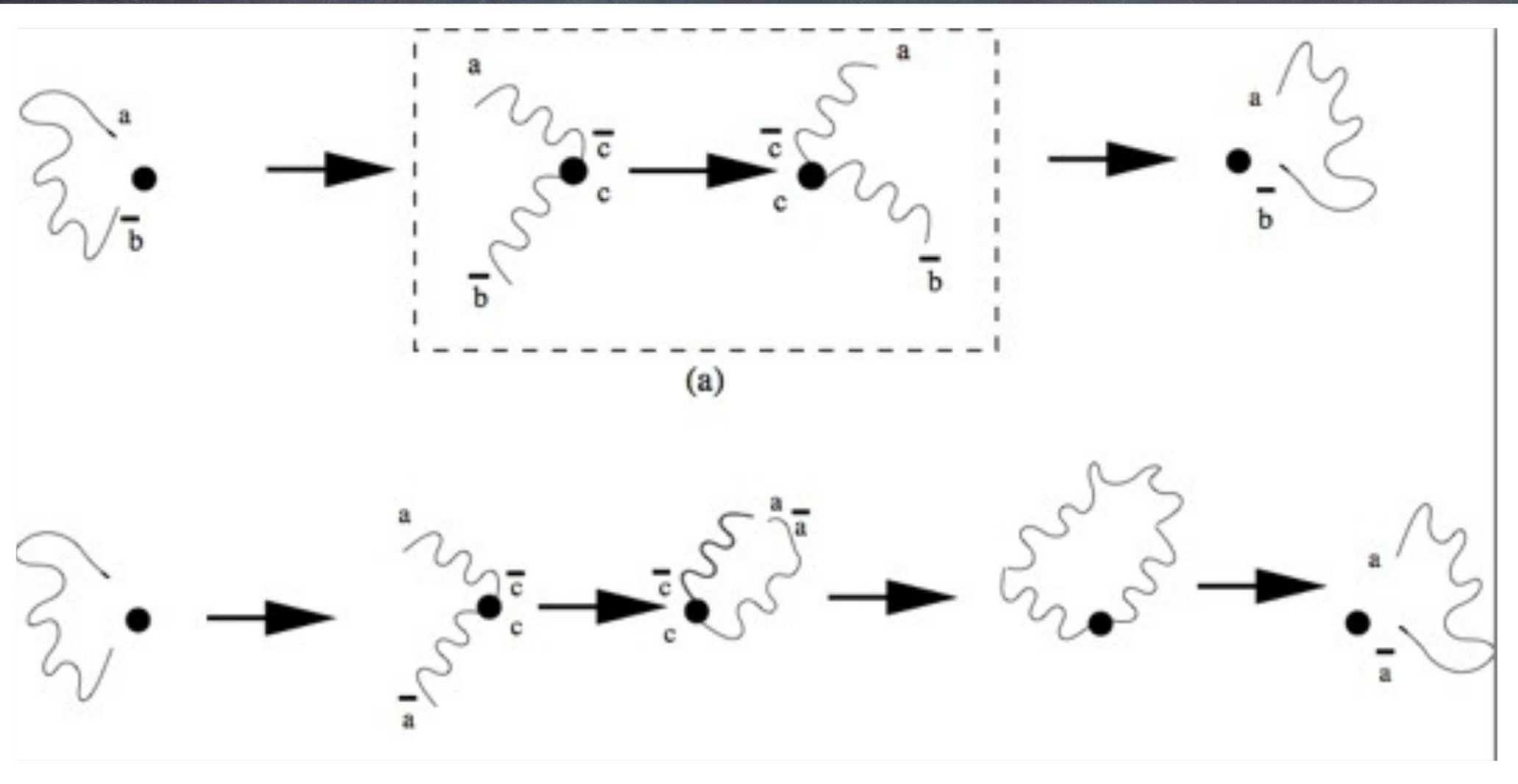


But the UHE photon limits are inconsistent with interpretations of time delays of high energy gamma-rays from GRBs within quantum gravity scenarios based on effective field theory

Maccione, Liberati, Sigl, PRL 105 (2010) 021101

Possible exception in space-time foam models,

Ellis, Mavromatos, Nanopoulos, arXiv:1004.4167



Conclusions

- 1.) The sources of ultra-high energy cosmic rays are still not identified due to rather small anisotropies; they are influenced by the source distribution and magnetic fields
- 2.) composition seems to become heavier at the highest energies which appears economic in terms of shock acceleration power
- 3.) The observed X_{\max} distribution of air showers also provides potential constraints on hadronic interaction models; however, more muons are observed than predicted by conventional models; this is hard to explain within the Standard Model
- 4.) Highest energy particles can be used as sensitive probes of the Lorentz symmetry